Vol1 No1
July 2021
e-ISSN: 2682-9177

AJMed TECH

ASIAN JOURNAL OF MEDICAL TECHNOLOGY

https://doi.org/10.32896/ajmedtech.v1n1

Numerical simulation of blood flow in cerebral aneurysms using two-phase model | Load bearing analysis on lumbosacral disc in pre-operative and post-operative thoracic scoliosis patient. | Application of digital signal processing and machine learning for electromyography: a review | Musculoskeletal disorder analysis-advanced in medical technology: review. | Development on sleep monitoring system configuration toward an optimal ambient condition setting of the sleep quality

https://ajmedtech.com

eISSN 2682-9177
9 772682 917006

Editorial Team

Editor-in-Chief

Prof. Dr. Ahmad Sobri Muda (Malaysia); Medical

Assoc. Prof. Ir. Ts. Dr. Abdul Rahim Abdullah (Malaysia); Technology

Managing Editor

Ts. Dr. Norhashimah Mohd Saad (Malaysia)

Assoc. Prof. Dr. Noramaliza Mohd Noor (Malaysia)

Editorial Board

Ir. Dr. Anis Suhaila Shuib (Malaysia)

Dr. Norihan Abdul Hamid (Malaysia)

Assoc. Prof. Dr. Wira Hidayat Mohd Saad (Malaysia)

Dr. Norhidayah Mohamad Yatim (Malaysia)

Dr. Anas Tharek (Malaysia)

ASIAN JOURNAL OF MEDICAL TECHNOLOGY

Contents

Volume 1 **Number 2** **July 2021**

No. ***Title*** ***Page***

balt solutions
for AVM treatment

squid
EVOH co-polymer

sonic
detachable tip microcatheter

balt
inspiring innovation

Join us for Hands-On
AVM Workshops. Register your interest with
carlteh@medcinpharma.com / hiba@medcinpharma.com

SQUID is a non-adhesive liquid embolic agent indicated for embolization of lesions in the peripheral and neurovasculature, including arteriovenous malformations and hypervascular tumors. Class III CE 0459 in compliance with Medical Device Directive (MDD 93/42/EEC amended by 2007/47/ EC. Manufactured by EMBO-FLUSSIGKEITEN AG. Route des Avouillons 30, CH-1196 GLAND, Switzerland. Carefully read the instruction of use before use. First CE marking:2012. SONIC is a reinforced microcatheter indicated in selective and hyperselective vascular catheterization for diagnostic or therapeutic purposes. Class III CE 0459 in compliance with Medical Device Directive (MDD 93/42/EEC amended by 2007/47/ EC. Manufactured by BALT Extrusion. Carefully read the instruction of use before use. First CE marking:2012. The content of this document, in particular data, information, trademarks and logos is BALT SAS's sole property. © 2018 BALT SAS and affiliates, all rights reserved. All representation and/or reproduction, whether in part or in full, is forbidden and would be considered a violation of BALT SAS and its affiliates' copyrights and other intellectual proprietary rights. This document with associated pictures is non-contractual and is solely dedicated to healthcare professionals and BALT's distributors (BALT's supplier's distributors).
The products commercialized by BALT shall exclusively be used in accordance with the instructions for use included in the boxes.

MEDCIN PHARMA SDN BHD (587084 - D)

Imported and distributed by :
Medcin Pharma Sdn Bhd (587084-D)
H-G-3A, Blok H, Sekitar 26 Enterprise,
Persiaran Hulu Selangor, Seksyen 26,
40400 Shah Alam, Selangor Darul Ehsan
Tel: +60 (03) 5192 3966
Fax: +60 (03) 5191 9539
http://www.medcinpharma.com

NUMERICAL SIMULATION OF BLOOD FLOW IN ANEURYSMS USING A TWO-PHASE MODEL

Md Al Amin Sheikh[1], Anis Suhaila Shuib[2] Mohd Hardie Hidayat Mohyi[2], Julaiha Adnan[3] and Ahmad Sobri Muda[4]

[1]School of Integrative and Global Majors, University of Tsukuba, 1-1-1 Tennodai, Tsukuba, 305-8577, Ibaraki, Japan

[2]School of Computer Science and Engineering, Taylors University, No 1, Jalan Taylors, 47500 Subang Jaya, Selangor, Malaysia

[3]Industrial Innovation Centre in Biomedical, SIRIM Industrial Research, SIRIM Berhad, Lot 5285, Lebuhraya Sg. Besi-Puchong, Sg.Besi, 57000 Kuala Lumpur, Malaysia

[4]Radiology Department, Hospital Pengajar Universiti Putra Malaysia, Faculty of Medicine and Health Sciences, UPM 43400 Serdang, Selangor, Malaysia

Corresponding Author's Email: [1]s2130538@u.tsukuba.ac.jp

Article History: Received April 14, 2021; Revised June 8, 2021; Accepted June 14, 2021

ABSTRACT: Computational fluid dynamics is utilized to understand the hemodynamics of aneurysms. In this study, two-phase blood flow was numerically simulated by a discrete phase model using the Lagrangian approach, with the blood cells representing the particulate phase and the plasma representing the continuous phase. Three patient-specific aneurysm geometries, namely, two saccular aneurysms located in the bifurcation of the basilar artery and one fusiform aneurysm located at the bifurcation of the common carotid artery and of the external carotid artery, were investigated. Wall shear stress (WSS), oscillatory shear index (OSI), and relative residence time (RRT) were determined from the simulation. The two-phase blood flow simulation revealed a high WSS (>3.0 Pa), a high OSI (>0.2), and a long RRT (>8) in the medium- and giant-sized saccular aneurysms. By contrast, a low OSI, a low WSS, and a short RRT were observed at the aneurysm dome of the fusiform aneurysm. However, at the bifurcation point, a high WSS and a long RRT with low oscillation were observed.

***KEYWORDS**: Aneurysm; Two-phase blood; Wall shear stress; Oscillatory shear*

index; Relative residence time

1.0 1.0 INTRODUCTION

A cerebral aneurysm is characterized by a bulging along the wall of a blood vessel in the brain. Such a condition weakens the vessel wall; moreover, aneurysms in cerebral arteries demonstrate the risk of rupturing or bursting [1], which would cause bleeding in the brain, known as hemorrhagic stroke. Understanding the mechanism of brain aneurysm rupture has been critical in finding the treatment to avoid the possible onset of fatal events [2]. Globally, nearly 500,000 deaths each year are caused by cerebral aneurysms [3].

Gaining an understanding of the biomechanics of blood flow is essential. Hemodynamics play a vital role in the formation, growth, and rupture of cerebral aneurysms [4]. Hemodynamics refers to the hydrodynamics of flow in blood vessels. It relates to the forces at play in blood flow. Several hemodynamic parameters are widely used in rupture risk analysis, in monitoring aneurysm growth, and in identifying atherosclerosis lesions; moreover, these parameters are used as indicators when determining the location where aneurysm formation would peak [5] [6] [7] [8].

Over the last two decades, computational fluid dynamic (CFD) techniques have been widely used to investigate the initiation, growth, and rupture of cerebral aneurysms [9]. Rupture risk prediction has been extensively investigated using CFD simulation wherein blood has been analyzed using a single-phase flow model, which considers hemodynamic parameters, such as wall shear stress (WSS) and oscillatory shear index (OSI); relative residence time (RRT) is a parameter that has been less investigated [8] [10]. In single-phase blood flow models, blood is treated both as a Newtonian and a non-Newtonian fluid in order to understand the development, growth, and rupture of cerebral aneurysms [11] [12]. Blood has also been analyzed using a multiphase flow model, wherein red blood cells (RBCs), white blood cells (WBCs), and platelets are considered to be suspended in the plasma. Additionally, in one study, cell transport, interactions, and low WSS distribution in leukocytes were analyzed in four patient-specific aneurysm geometries [13].

In this study, blood was considered as a two-phase fluid, with plasma as the continuous phase and RBCs as the particulate phase. The continuous phase was solved using the Naiver–Stokes equation, and

the particulate phase was solved using the discrete phase model (DPM). This research aims to determine the WSS, OSI, RRT, velocity streamlines, and surface velocities in aneurysms by using a two-phase blood flow model.

2.0 METHODS

2.1 Equations and validation of the DPM

The ANSYS-Fluent simulation package with DPM was utilized to solve the motion of plasma and RBCs using the Lagrangian approach, wherein blood trajectories were calculated. The continuous fluid was first solved according to the Naiver–Stokes equation, and the particulate phase in the plasma was solved using the DPM. The individual particles were tracked by calculating the fluid flow field. Each particle was analyzed computationally at certain time intervals during the fluid phase calculation. The trajectory equation was solved through stepwise interactions over discrete time steps. The integration of time yielded the velocity of the particle at each point along the trajectory.

In the DPM, the blood cells were considered rigid particles. The movement of blood cells is governed by particle motion. The equation for particle motion was fundamentally derived from Newton's laws of motion, where the resultant of all the forces ΣF acting on particles' mass m is proportional to the acceleration a of the particles, and each action has a reaction that is equal in magnitude but acting in the opposite direction.

$$\Sigma F = ma \tag{1}$$

The motion of a spherical particle in a fluid is expressed as follows:

$$m_p \frac{\partial u_p}{\partial t} = m_p \left(1 - \frac{\rho}{\rho_n}\right) g + F_{pg} + F_D + F_L + F_{vm} + F_{Bas} \tag{2}$$

where m_p is the mass of the particle, u_p is the instantaneous velocity of the particle, g is the body acceleration, F_D is the drag force, F_L is the lift force generated by the rotation of a particle and shear flow, F_{pg} is the force that exists in the absence of a particle due to the acceleration of the fluid and due to the hydrostatic pressure gradient, F_{vm} is the virtual mass force that accounts for the work required to change the momentum of the surrounding fluid as particles accelerate, and F_{Bas} is the unsteady drag force or Basset force that accounts for the temporal development of the viscous region that affects the velocity of the particles.

An equal balance between particles' mass acceleration and the action forces was used to determine the movement of each particle in the disbanded phase. In this research, we presumed the force as a drug-related force, whereas all other forces were considered small and negligible [14]. The governing equation is as follows:

$$m_p \frac{\partial u_p}{\partial t} = m_p + \left(1 - \frac{\rho}{\rho_n}\right) g + F_D \tag{3}$$

where F_D is the per unit mass drag force and is derived as

$$F_D = \frac{18\mu}{\rho_n d_n^2} \frac{C_d Re_p}{24} (u - u_p) \tag{4}$$

where u is the fluid velocity, ρ is the fluid density, ρ_p is the particle density, d_p is the particle density, C_d is the drag coefficient, and Re_p is the relative Reynolds number, which is expressed as

$$Re_p = \frac{\rho a_{p|u-u_p|}}{\mu} \tag{5}$$

The CFD software uses the empirical approach described by Morsi and Alexander [15] to determine the drag coefficient, which is defined as follows:

$$C_d = \omega_1 + \frac{\omega_2}{Re_n} + \frac{\omega_3}{Re_n^2} \tag{6}$$

where ω_1, ω_2, and ω_3 are the constants that are appropriate for the spherical particles at different Reynolds numbers. The particle trajectory equation is expressed as follows:

$$\frac{\partial x_i}{\partial t} = u_{p.i} \tag{7}$$

The particle time is t, and x_i is the position coordinate, as described by Dhahbi et al. 2012 [14]. The interaction of the injected particle with the continuous phase was specified, and 10 continuous phase iterations per DPM iteration were defined per the software guidelines [16].

To validate the DPM, we performed CFD simulation by benchmarking with an experimental study [17], along with the CFD results for patient-specific cerebral aneurysms and arterial blockage [13] [18] [19]. Also, a numerical validation of the DPM was published elsewhere [21]. In the validation study, blood was divided into two major components: water and RBCs. Human RBCs, which had a density of 1130 kgm^{-3} and a diameter of 7.5 μm, were considered as rigid particles that are suspended in water, which had a density and viscosity of 1000 kgm^{-3} and 0.001 Pa·s, respectively [20] . Two inlet

velocities, 0.0757 ms^{-1} and 0.233 ms^{-1}, were chosen; the fluid flow was considered Newtonian with a steady-state flow. As shown by theoretical and experimental studies, the reattachment point plays an important role in the numerical validation of the DPM. Figure 1 compares the reattachment points obtained in an experimental work, in two computational studies, and in the current computational investigation. The validated DPM model was used in this simulation.

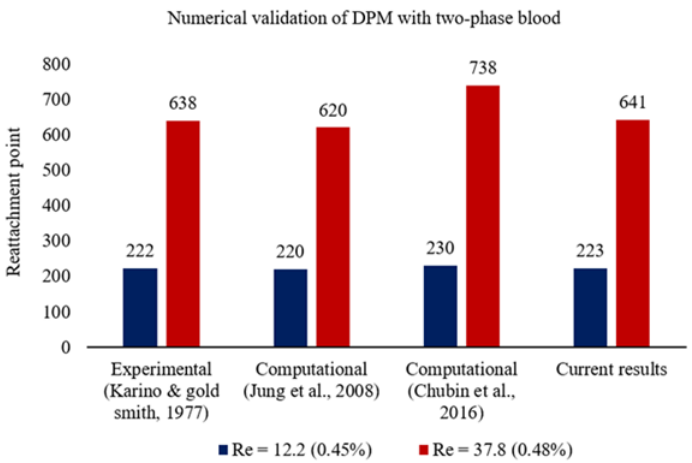

Figure 1: Numerical validation of the DPM, wherein the current results are compared with previous findings.

2.2 Patient-specific aneurysm geometries

Three patient-specific aneurysm geometries were selected to determine the rupture risk of cerebral aneurysms. These patient-specific aneurysm geometries were segmented and constructed from 3D rotational computed tomography angiography (CTA) images to generate 3D geometries using the medical research software Materialise Mimics 22.0 and 3-Matic 20.0. Data were obtained from the Radiology Department, Faculty of Medical and Health Sciences, Universiti Putra Malaysia. The segmented aneurysm geometries denoted as geometry 1, geometry 2, and geometry 3, are shown in Figure 2a, 2b, and 2c, respectively.

The aneurysm geometries 1 and 3 were saccular aneurysms located in the bifurcation of the basilar artery (BA) to the posterior communicating arteries. The aneurysm geometry 2 was a fusiform aneurysm located at the bifurcation of the common carotid artery (CCA) and external carotid artery. However, missing information in the CTA images in aneurysm case 3, that is, the outlet 1 artery with aneurysm geometry, was reconstructed for further investigation.

2.3 CFD method

The Ansys-Fluent 2019 R3 was used for the CFD analysis of the patient-specific aneurysm geometries. An unstructured tetrahedral mesh with a maximum element size of 0.15 mm with a four-layer prism mesh was applied after completing the mesh independence test. The meshed aneurysm geometry 2 is shown in Figure 2d to 2f. The continuous phase was the plasma, which had a density of 1020 kgm^{-3} and a viscosity of 0.002 Pa·s. The particulate phase had a mean diameter of 8.2 μm and a density of 1100 kgm^{-3} [17].

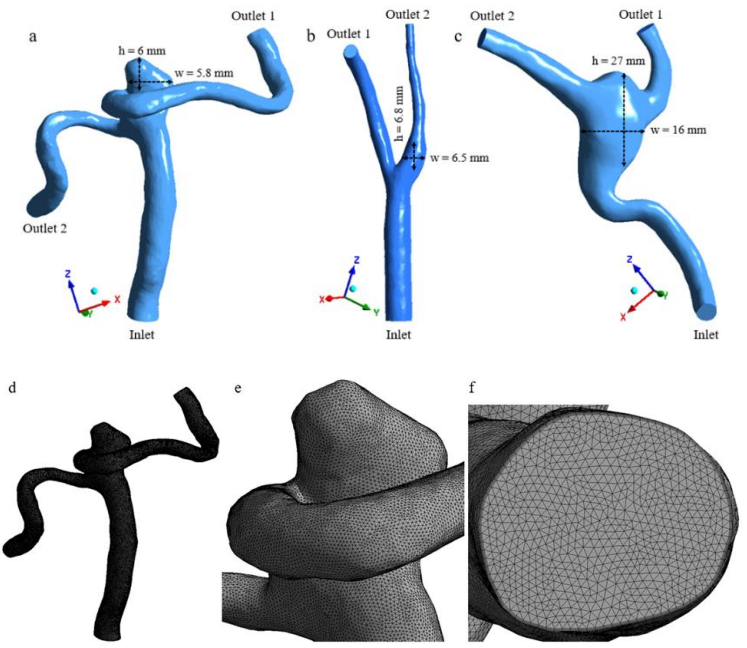

Figure 2: Patient-specific aneurysm geometries. (a) Geometry 1 (height (h) = 6 mm; width (w) = 5.8 mm); (b) geometry 2 (h = 6.8 mm; w = 6.5 mm); and (c) geometry 3 (h = 27 mm; w = 16 mm). Meshed aneurysm geometry 1: (d) full geometry of the unstructured tetrahedral mesh, (e) aneurysm body mesh, and (f) inlet meshing with a four-layer prism mesh.

The blood flow in the aneurysm was modelled to be incompressible. A pressure-based solver was selected for the simulation. The Semi-Implicit Method for Pressure Linked Equation (SIMPLE) scheme was used for pressure–velocity coupling. A 1s pulsatile inlet velocity profile was defined and written as the user-defined function in the c programming language [22]. Figure 3a presents the inlet pulsatile

velocity profile. Zero pressure was applied in the outlet boundary condition. Ten cardiac cycle simulations were performed for each aneurysm geometry with a time-step of 0.005 s, as shown in Figure 3b. Each time-step convergence achieved a minimum residual of 10^{-4}.

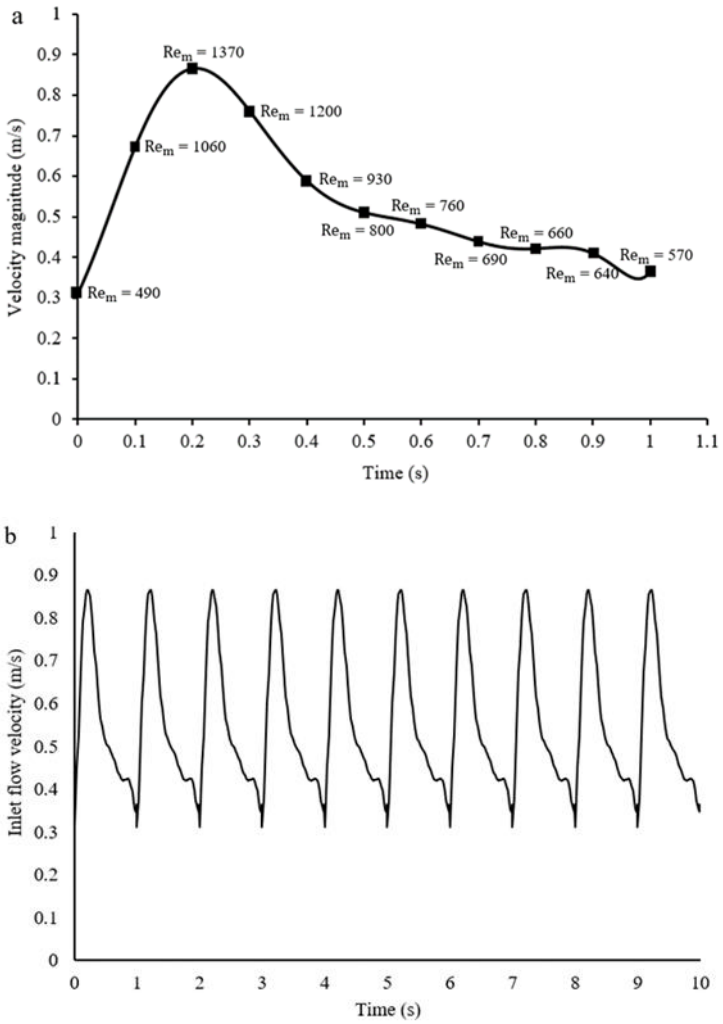

Figure 3: Inlet pulsatile velocity profile. (a) 1s inlet pulsatile velocity with mean Reynolds number. (b) Inlet flow velocity in 10 cardiac cycles.

The Reynolds number was based on the parent artery's mean inlet diameter and was calculated using the following equation:

$$Re_m = \frac{\rho D_{mean} V}{\mu} \quad (8)$$

where ρ is the density of the fluid, D_{mean} is the mean diameter of the parent blood vessels inlet, V is the velocity of the fluid, and μ is the fluid viscosity. The mean Reynolds numbers Re_m of the three aneurysm geometries ranged from 490 to 1370. The data were based on the mean Reynolds number obtained in the simulation that involved 10 cardiac cycles.

The hemodynamic parameters obtained from the simulation were WSS (calculated as the ratio of the time-averaged WSS of the last cardiac cycle to the average WSS of the parent artery), OSI (a non-dimensional parameter calculated based on the directional changes in WSS), and RRT (residence time of blood cells near the artery of the aneurysm wall). To analyze the velocity distribution inside the aneurysm, we retrieved the velocity streamline and surface velocity data for all aneurysm geometries.

3.0 RESULTS

The two-phase blood was solved with the DPM and completed in 10 cardiac cycles. After the simulation for 10 cardiac cycles, a total of 145,865 RBCs for aneurysm geometry 1, 160,245 RBCs for aneurysm geometry 2, and 185,715 RBCs aneurysm geometry 3 were tracked.

Large aneurysms possibly have a higher risk of rupture compared with the small ones [23]. According to Lee et al. 2015 [24], aneurysm sizes are classified based on the maximum dimension of aneurysm geometries. The size categories are as follows: small (0 mm to 4.9 mm), medium (5 mm to 9.9 mm), large (10 mm to 24 mm), and giant (>25 mm). On this basis, the aneurysm geometries 1 and 2 were classified as medium-sized aneurysms, whereas geometry 3 was classified as a giant aneurysm. The height and width of the aneurysm geometries are presented in Figure 3. WSS, OSI, RRT, velocity streamlines, and surface velocities for the last cardiac cycle for geometries 1, 2, and 3 are plotted in Figures 4, 5, and 6, respectively.

WSS is an essential hemodynamic parameter and is categorized as either high or low. A low WSS is characterized by <1 Pa, whereas a high WSS is characterized by >3 Pa [23]. In the two-phase blood flow simulation, the high WSS values were observed in aneurysm geometries 1 and 3, and a low WSS was observed in the aneurysm dome of geometry 2, as shown in Figures 4a, 6a, and 5a, respectively. A high WSS was observed at the bifurcation in aneurysm 2.

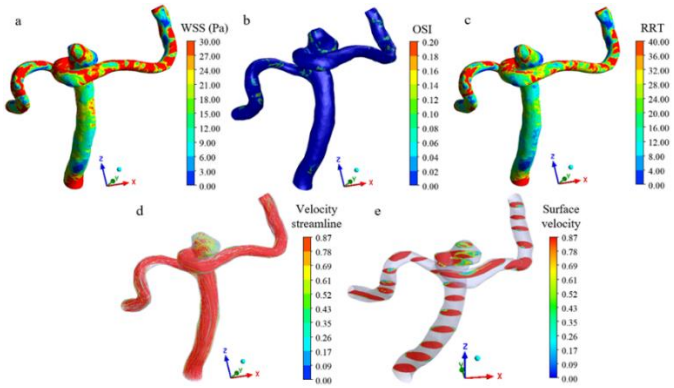

Figure 4: Geometry 1: Medium-sized saccular aneurysm in the BA. (a) WSS. (b) OSI. (c) RRT. (d) Velocity streamlines. (e) Surface velocities.

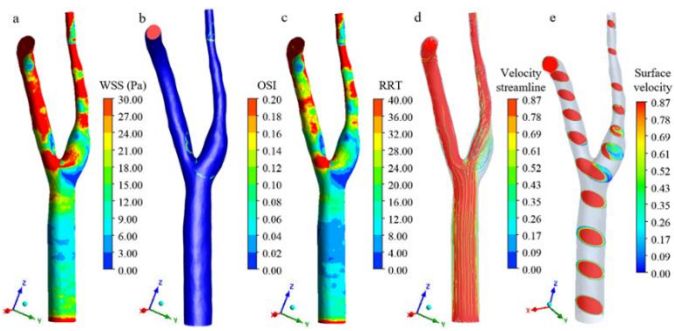

Figure 5: Geometry 2: Medium-sized fusiform aneurysm in the bifurcation of the CCA. (a) WSS. (b) OSI. (c) RRT. (d) Velocity streamlines. (e) Surface velocity.

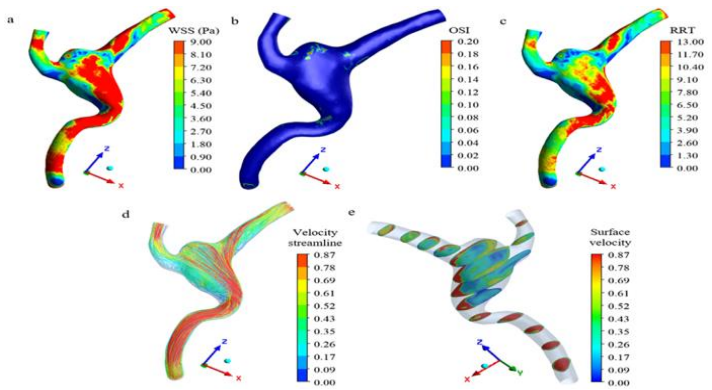

Figure 6: Geometry 3: Giant saccular aneurysm in the BA. (a) WSS. (b) OSI. (c) RRT. (d) Velocity streamlines. (e) Surface velocity.

The OSI, which ranges from 0 to 0.2, indicates the directional changes in the WSS. Zero indicates no oscillation, whereas 0.2 indicates high oscillation [24] [25]. High OSI values were observed in the aneurysm geometries 1 and 3, and a low OSI was observed in the aneurysm dome of geometry 2, as shown in Figures 4b, 6b, and 5b, respectively.

The RRT indicates the residence time of blood flow inside an aneurysm. A short RRT is indicated by values 0 to 7, whereas values >8 indicate a long RRT [26]. A long RRT was observed in the aneurysm geometries 1 and 3, whereas a low RRT was observed in the aneurysm dome of geometry 2, as shown in Figures 4c, 6c, and 5c, respectively. Also, a long RRT was observed at the bifurcation of geometry 2.

Overall, a high WSS, a high OSI, and a long RRT were observed in the aneurysm dome of geometries 1 and 3. In geometry 2, a low WSS, a low OSI, and a short RRT were observed in the aneurysm dome, whereas a high WSS and a long RRT were observed at the vessel bifurcation point.

Velocity streamline and surface velocity were calculated to analyze the velocity distribution inside the aneurysms. To calculate the velocity distribution inside the aneurysm, we calculated the contour between 0 and 0.865 ms^{-1}. The velocity streamline indicates the blood flow circulation inside the aneurysms. Figures 4d and 4e show the changes in velocity streamline and surface velocity, respectively, for the aneurysm geometry 1. As blood was recirculating, and variable high velocities were observed based on the velocity streamline and surface velocity changes in the aneurysm dome. For the aneurysm geometry 2, the velocity streamline indicates the flow stagnation in aneurysm shown in Figure 5d. Changes in surface velocity were observed in the aneurysm, and the middle surface of the aneurysm demonstrated low-

velocity values, as depicted in Figure 5e. As displayed in Figure 6d, flow disturbance and recirculation were observed in geometry 2, which is a giant aneurysm in the BA. The high velocity in the aneurysm dome is shown in Figure 6e.

4.0 DISCUSSION

Hemodynamics is important in predicting the risk of aneurysm rupture in cerebral arteries when using a single-phase blood flow model. WSS, OSI, and RRT are the key hemodynamic parameters that are directly related to aneurysm rupture risk in cerebral arteries [28]. However, in a single-phase, blood flow simulation, variations in high and low WSS values were not comprehensively investigated as to whether they describe the properties of a Newtonian and a non-Newtonian fluid [25]. In this study, a two-phase blood flow simulation was performed using three patient-specific aneurysm geometries. The two-phase blood that consists of plasma and RBCs plays an essential role in predicting rupture risk, which is indicated by a high WSS, a high OSI, and a long RRT. Jung et al. 2008 [18] observed a high velocity with high WSS values in plasma containing RBCs, whereas a low WSS was observed in WBCs in the multiphase blood flow model of Chubin et al. 2016 [13]. A high WSS, a high OSI, and a long RRT may be associated with a high risk of aneurysm rupture in cerebral arteries.

WSS is an essential hemodynamic parameter in rupture risk prediction in brain vessels with an aneurysm. For the rupture risk analysis, WSS was calculated mainly using the normalized WSS and time-averaged WSS in cerebral arteries with aneurysms [5] [24]. The WSS contour value was normalized based on the actual WSS values, and the values obtained ranged from 0 to 1 or 2.5 [24] [29]. The time-averaged WSS was calculated using the characteristics of an entire-time cycle and was measured in pascal, with normal values ranging from 1.5 to 10 based on the absolute time-averaged magnitude of each wall mesh point vector [5]. As for the WSS in brain vessels with aneurysms, the contour value of the WSS is influenced by various parameters, such as blood vessel geometry, meshing, and blood cell properties. Usually, the blood pressure is 10,000 Pa when the WSS of the wall of a healthy vessel is 0 Pa to 20 Pa [30]. Valen-Sendstad et al. 2011 [22] simulated the average pulsatile blood flow in a middle cerebral artery aneurysm. The WSS contour was 0 Pa to 48 Pa based on the average pulsatile blood. In the aneurysm wall, the normal WSS values were 0 Pa to 1.5 Pa, and a WSS of 1.5 Pa to 2.0 Pa indicated a high risk of rupture. A value greater than 3.0 Pa is considered a high WSS [31].

Some studies have found that both high and low WSS were related to aneurysm growth and rupture [23]. However, the present study focuses on high WSS values in the aneurysm wall because the two-phase blood plasma containing RBCs is associated with high WSS.

High WSS in turn is associated with positive WSS gradient resulting from endothelial cell damage, matrix metalloproteinase production by mural cells, extracellular matrix degradation, thinning of media, and apoptosis of smooth muscle cells and fibroblasts, and such an association further increases the risk of aneurysm rupture [27].

OSI, a non-dimensional parameter whose value ranges from 0 to 0.5, is used to calculate the directional changes in WSS in a cardiac cycle. In this study, OSI ranged from 0 to 0.2, consistent with the findings of previous studies, where 0 represents a steady flow and 0.2 represents a high oscillation in aneurysm geometries [25]. In an aneurysm, OSI indicates several directional changes throughout a cardiac cycle. A low OSI may promote atherogenesis and inflammatory diseases and may lead to intimal wall thickening [27] [32] [26]. However, in several studies, a high OSI has been observed in ruptured aneurysms, and it has been an independent risk factor in aneurysm rupture risk prediction [27] [26] [33].

The RRT is the residence time of blood near the aneurysm wall. The RRT was based on a low WSS and a high OSI inside the aneurysm. Long-term circulation of blood flow near the aneurysm wall could lead to the rupture of an aneurysm. A study involving 30 aneurysm cases investigated the RRT, which is an essential indicator of atherosclerotic changes in cerebral aneurysms [34]. The occurrence of a low WSS with long RRT was investigated in atherosclerotic and non-atherosclerotic aneurysms, respectively; long RRT was observed in atherosclerotic aneurysms but not in non-atherosclerotic aneurysms [7]. However, knowledge on the association between a high WSS with a long RRT and the high risk of rupture remains limited. The long residence time of blood cells triggers the cellular interaction that promotes blood clotting and wall dilation. A high WSS with a long RRT is a key indicator that leads to a high risk of aneurysm rupture in cerebral arteries.

Table 1 presents the rupture risk assessment of the aneurysm geometries based on WSS, OSI, and RRT with mean Reynolds number. The simulation results for the last cardiac cycle are based on the inlet mean Reynolds number, which indicates the risk (i.e., high or low) of aneurysm rupture. The aneurysm geometries 1 and 3 demonstrate a high risk of rupture compared with the aneurysm geometry 2. In geometry 2, a high WSS, a low OSI, and a long RRT were observed at the vessel bifurcation point. According to Soldozy et al. 2019 [27], an aneurysm has a low risk of rupture, but further growth of the aneurysm could be anticipated.

Table 1: Rupture risk analysis of the aneurysm geometries based on the changes in WSS, OSI, and RRT with mean Reynolds number.

Aneurysm geometries	WSS	OSI	RRT	Analysis
Aneurysm geometry 1	High WSS at Re_m in between 1200 to 1370	High OSI at Re_m = 1060, 1200, 760, and 660	Long RRT Re_m: 1200 < Re_m < 1370	High risk of rupture
Aneurysm geometry 2 (aneurysm dome)	Low WSS	Low OSI	Short RRT	Low risk of rupture
Aneurysm geometry 2 (vessel bifurcation point)	High WSS at Re_m in between 1200 to 1370	Low OSI	Long RRT Re_m: 1200 < Re_m < 1370	Low risk of rupture. Aneurysm growth may occur.
Aneurysm geometry 3	High WSS at Re_m in between 800 to 1370	High OSI at Re_m = 1370, 1060, 930, 760, and 690	Long RRT Re_m: 1200 < Re_m < 1370	High risk of rupture

Previously, a high WSS, a high OSI, and a long RRT were reported as key indicators that are highly associated with a damaged artery wall and that may promote aneurysm rupture [27] [26] [31].

5.0 LIMITATION

This study has some limitations. The 3D rotational CTA images had a limited quality, lacked some information, and could not render a perfect 3D geometry of cerebral arteries with an aneurysm. A minor part of the geometry was assumed. Small blood vessels were not considered in the 3D geometry of the cerebral arteries with an aneurysm. The effect of the entire flow was assumed to be small and negligible. Due to the lack of experimental studies involving a two-phase blood model, experimental data that were obtained within the laminar flow region were selected. Moreover, only three patient-specific aneurysm geometries were selected for the numerical simulation of the two-phase blood flow model, but these three geometries may not generally represent the entire population of cerebral artery aneurysms. The two phases of blood, namely, plasma and RBCs, were considered in this study; the WBCs were not considered and were assumed as not having a significant impact on the flow given that their volume percentage is 1% compared with that of RBCs, which is typically 45%. In the current DPM simulation, the RBCs were assumed to be rigid spherical particles. RBC agglomerations were neglected and were considered as simply spherical particles. The number of particles injected ranged from 145,865 to 185,715, which is possibly lower than the actual number of RBCs in the blood. The two-phase blood flow was solved in a continuous phase using the Navier–

Stokes equation, and the particulate phase was solved with the DPM using the Lagrangian frame approach. The discrete phase trajectory was calculated using the formulation that included the discrete phase inertia and drag force. The zero-pressure outlet for the boundary conditions was chosen due to the limitation in obtaining the actual pressure data. The vessel wall was considered rigid with a no-slip boundary condition. Moreover, rupture risk was predicted based on published values. A high risk of rupture was associated with high WSS, high OSI, and long RRT. In the analysis of rupture risk, low WSS was indicated by <1 Pa, whereas high WSS was indicated by >3 Pa in the brain vessel. OSI indicated the directional changes in WSS, and it ranged between 0 and 0.2, where 0 indicated no oscillation and 0.2 indicated a high oscillation. RRT was either long or short based on the contour value. A contour value between 8 and 14 indicated a long RRT, whereas a value of 7 or less indicated a short RRT.

6.0 CONCLUSION

The blood flow in the three aneurysm geometries was numerically simulated using the DPM, which considered the two-phase nature of blood. Three important hemodynamic parameters, namely, WSS, OSI, and RRT, were analyzed. The simulation of the two-phase blood flow revealed a high WSS (>3.0 Pa), a high OSI (>0.2), and a long RRT (>8) in medium- and giant-sized saccular aneurysms. In the investigated region, high stress, high flow oscillation, and flow recirculation may be associated with a high risk of aneurysm rupture. For a medium-sized fusiform aneurysm located in the CCA, a low OSI, a low WSS, and a short RRT were found at the aneurysm dome. The risk of rupture in the bulge area may be lower compare to other area. However, at the bifurcation point, a high WSS and a long RRT with low oscillation were observed. The aneurysm may tend to grow at the bifurcation area where velocity is high. The results suggested the need to comprehensively analyze the correlation between hemodynamic parameters and the risk of rupture. Given the limitations highlighted in this study, in-depth and detailed numerical simulation of a larger number of patient-specific geometries is warranted. This paper underscores the importance of biomechanical forces in the risk of aneurysm rupture.

7.0 DECLARATION OF COMPETING INTEREST

The authors declare that they have no known competing financial interests or personal relationships that could have appeared to influence the work reported in this paper.

8.0 ACKNOWLEDGMENTS

The authors acknowledge the financial support provided by Taylor's

University Malaysia through Taylor's University Flagship Research Programme (TUFR) and Taylor's Research Excellence Scholarship.

9.0 REFERENCES

[1] N. Chalouhi, B. L. Hoh, and D. Hasan, "Review of cerebral aneurysm formation, growth, and rupture," *Stroke*, vol. 44, no. 12, pp. 3613–3622, 2013.

[2] J. Menke, J. Larsen, and K. Kallenberg, "Diagnosing cerebral aneurysms by computed tomographic angiography: meta-analysis," *Ann. Neurol.*, vol. 69, no. 4, pp. 646–654, 2011.

[3] A. I. Shehata, T. Hassan, and K. M. Saqr, "Effects of Non-Newtonian Viscosity on the Hemodynamics of Cerebral Aneurysms," *Appl. Mech. Mater.*, vol. 819, pp. 366–370, 2016.

[4] M. Longo *et al.*, "Role of Hemodynamic Forces in Unruptured Intracranial Aneurysms: An Overview of a Complex Scenario," *World Neurosurg.*, vol. 105, pp. 632–642, 2017.

[5] S. Omodaka *et al.*, "Local hemodynamics at the rupture point of cerebral aneurysms determined by computational fluid dynamics analysis," *Cerebrovasc. Dis.*, vol. 34, no. 2, pp. 121–129, 2012.

[6] A. Mantha, C. Karmonik, G. Benndorf, C. Strother, and R. Metcalfe, "Hemodynamics in a cerebral artery before and after the formation of an aneurysm," *Am. J. Neuroradiol.*, vol. 27, no. 5, pp. 1113–1118, 2006.

[7] S. Sugiyama *et al.*, "Computational hemodynamic analysis for the diagnosis of atherosclerotic changes in intracranial aneurysms: a proof-of-concept study using 3 cases harboring atherosclerotic and nonatherosclerotic aneurysms simultaneously," *Comput. Math. Methods Med.*, vol. 2016, 2016.

[8] N. Varble, K. Kono, H. Rajabzadeh-Oghaz, and H. Meng, "Rupture Resemblance Models May Correlate to Growth Rates of Intracranial Aneurysms: Preliminary Results," *World Neurosurg.*, vol. 110, pp. e794–e805, 2018.

[9] P. M. Munarriz, P. A. Gómez, I. Paredes, A. M. Castaño-Leon, S. Cepeda, and A. Lagares, "Basic Principles of Hemodynamics and Cerebral Aneurysms," *World Neurosurg.*, vol. 88, pp. 311–319, 2016.

[10] Y. Wang, X. Leng, X. Zhou, W. Li, A. H. Siddiqui, and J. Xiang, "Hemodynamics in a middle cerebral artery aneurysm before its growth and fatal rupture: Case study and review of the literature," *World Neurosurg.*, vol. 119, pp. e395–e402, 2018.

[11] G. Carty, S. Chatpun, and D. M. Espino, "Modeling blood flow through intracranial aneurysms: A comparison of Newtonian and non-Newtonian viscosity," *J. Med. Biol. Eng.*, vol. 36, no. 3, pp. 396–409, 2016.

[12] A. Valencia, H. Morales, R. Rivera, E. Bravo, and M. Galvez, "Blood flow dynamics in patient-specific cerebral aneurysm models: the relationship between wall shear stress and aneurysm area index," *Med. Eng. Phys.*,

vol. 30, no. 3, pp. 329–340, 2008.
[13] C. Ou, W. Huang, M. M. F. Yuen, and Y. Qian, "Hemodynamic modeling of leukocyte and erythrocyte transport and interactions in intracranial aneurysms by a multiphase approach," *J. Biomech.*, vol. 49, no. 14, pp. 3476–3484, 2016.
[14] M. Dhahbi, M. Ben Chiekh, B. Gilles, J. C. Béra, and A. Jemni, "Numerical simulations of particle dynamics in a poststenotic blood vessel region within the scope of extracorporeal ultrasound stenosis treatment," *Med. Eng. Phys.*, vol. 34, no. 7, pp. 982–989, 2012.
[15] S. A. J. Morsi and A. J. Alexander, "An investigation of particle trajectories in two-phase flow systems," *J. Fluid Mech.*, vol. 55, no. 2, pp. 193–208, 1972.
[16] I. ANSYS, "Fluent 6.2 User's Manual." ANSYS, Inc. Canonsburg, PA, 2005.
[17] T. Karino and H. L. Goldsmith, "Flow behaviour of blood cells and rigid spheres in an annular vortex," *Philos. Trans. R. Soc. London. B, Biol. Sci.*, vol. 279, no. 967, pp. 413–445, 1977.
[18] J. Jung and A. Hassanein, "Three-phase CFD analytical modeling of blood flow," *Med. Eng. Phys.*, vol. 30, no. 1, pp. 91–103, 2008.
[19] K. Joisar, R. Bhoraniya, and A. Harichandan, "Numerical Analysis of Two-Phase Blood Flow in Idealized Artery with Blockage," in *Innovative Design, Analysis and Development Practices in Aerospace and Automotive Engineering (I-DAD 2018)*, Springer, 2019, pp. 259–267.
[20] S. K. Yu and H. L. Goldsmith, "Behavior of model particles and blood cells at spherical obstructions in tube flow," *Microvasc. Res.*, vol. 6, no. 1, pp. 5–31, 1973.
[21] P. A. Thrower, "global research conference (grace 2020)," 2020. .
[22] K. Valen-Sendstad, K.-A. Mardal, M. Mortensen, B. A. P. Reif, and H. P. Langtangen, "Direct numerical simulation of transitional flow in a patient-specific intracranial aneurysm," *J. Biomech.*, vol. 44, no. 16, pp. 2826–2832, 2011.
[23] H. Meng, V. M. Tutino, J. Xiang, and A. Siddiqui, "High WSS or low WSS? Complex interactions of hemodynamics with intracranial aneurysm initiation, growth, and rupture: toward a unifying hypothesis," *Am. J. Neuroradiol.*, vol. 35, no. 7, pp. 1254–1262, 2014.
[24] N. Varble *et al.*, "Shared and distinct rupture discriminants of small and large intracranial aneurysms," *Stroke*, vol. 49, no. 4, pp. 856–864, 2018.
[25] N. Varble, K. Kono, H. Rajabzadeh-Oghaz, and H. Meng, "Rupture resemblance models may correlate to growth rates of intracranial aneurysms: preliminary results," *World Neurosurg.*, vol. 110, pp. e794–e805, 2018.
[26] J. Xiang *et al.*, "Hemodynamic–morphologic discriminants for intracranial aneurysm rupture," *Stroke*, vol. 42, no. 1, pp. 144–152, 2011.
[27] S. Soldozy *et al.*, "The biophysical role of hemodynamics in the pathogenesis of cerebral aneurysm formation and rupture," *Neurosurg. Focus*, vol. 47, no. 1, p. E11, 2019.

[28] M. A. A. Sheikh, A. S. Shuib, and M. H. H. Mohyi, "A Review of Hemodynamic Parameters in Cerebral Aneurysm," *Interdiscip. Neurosurg.*, p. 100716, 2020.
[29] P. Jiang *et al.*, "Hemodynamic characteristics associated with thinner regions of intracranial aneurysm wall," *J. Clin. Neurosci.*, vol. 67, pp. 185–190, 2019.
[30] P. R. Hoskins and D. Hardman, "Three-dimensional imaging and computational modelling for estimation of wall stresses in arteries," *Br. J. Radiol.*, vol. 82, no. special_issue_1, pp. S3–S17, 2009.
[31] J. M. Dolan, J. Kolega, and H. Meng, "High wall shear stress and spatial gradients in vascular pathology: a review," *Ann. Biomed. Eng.*, vol. 41, no. 7, pp. 1411–1427, 2013.
[32] D. M. Sforza, C. M. Putman, and J. R. Cebral, "Hemodynamics of cerebral aneurysms," *Annu. Rev. Fluid Mech.*, vol. 41, pp. 91–107, 2009.
[33] T. Qiu, G. Jin, H. Xing, and H. Lu, "Association between hemodynamics, morphology, and rupture risk of intracranial aneurysms: a computational fluid modeling study," *Neurol. Sci.*, vol. 38, no. 6, pp. 1009–1018, 2017.
[34] S. Sugiyama *et al.*, "Relative residence time prolongation in intracranial aneurysms: a possible association with atherosclerosis," *Neurosurgery*, vol. 73, no. 5, pp. 767–776, 2013.

LOAD BEARING ANALYSIS ON LUMBOSACRAL DISC IN PRE-OPERATIVE AND POST-OPERATIVE THORACIC SCOLIOSIS PATIENT

Mohankumar Palaniswamy[1,*], Anis Suhaila Shuib[2], Shajan Koshy[2]

[1]Affiliation 1.
Physiotherapist, Chennai, 600032, Tamil Nadu, India.
[2]Affiliation 2.
Taylor's University, Subang Jaya 47500, Selangor, Malaysia.

[*]Corresponding Author's Email: [1]mohanphysionix06@live.com

Article History: Received May 30, 2021; Revised June 25, 2021; Accepted June 28, 2021

ABSTRACT: Scoliosis is a musculoskeletal disorder seen all around the world. It affects both the alignment of the vertebra and intervertebral disc. Scoliosis can be treated conservatively with a cast and brace or surgically with spinal instrumentation. During planning for surgical instrumentation, several factors need to be considered. Among those, biomechanical changes in the non-scoliotic vertebrae and discs are important. This is vital in determining the future degenerative changes of the spine. For this reason, this study was conducted with a finite element model of the lumbosacral joint using CT scan files to find the total deformation and equivalent static strain of the lumbosacral disc between pre and post-operative thoracic scoliosis patients. From the results, it is evident that there is a biomechanical change in the lumbosacral disc and structural change in the vertebral alignment followed immediately after corrective surgery. The correction in the alignment of the scoliotic spine brings changes to the biomechanical functionality and load-bearing capacity of the lumbosacral intervertebral disc before and after surgery.

***KEYWORDS**: Thoracic scoliosis, Lumbosacral disc, Finite element analysis, Vertebral alignment, Vertebral load.*

1.0 INTRODUCTION

The human vertebral column consists of 24 articulating and 9 fused vertebrae (7 cervical, 12 thoracics, 5 lumbar, 5 fused sacral, and 4 fused

coccyx vertebrae), which totals to 33 vertebrae. An intervertebral disc, held together by ligaments, separates the column formed by the articulating vertebra with the adjacent vertebra. This results in the formation of curves during weight-bearing. Scoliosis is a deformity of the vertebral column, in which the spine is abnormally twisted and curved to the sides. Globally scoliosis is one of the most common musculoskeletal disorders affecting the pediatric age group with a prevalence of 2-3%. When examining the spine from the back, a scoliotic spine will appear 'C' shaped (single curvature) or 'S' shaped (double curvature). It can be treated conservatively with a cast or brace or surgically with spinal instrumentation. Opting for surgical intervention depends upon various factors such as etiology, severity, cardiopulmonary involvement, Cobb's angle, and age. During spinal instrumentation surgery, surgeons fuse the scoliotic vertebrae using metal implants. Since the alignment of vertebrae is affected in scoliosis, the Center of Gravity (CoG) and Line of Gravity (LoG) is also affected. In an anatomical standing posture, the CoG and LoG lie anterior to the sacrum bone (S2). Whereas, in scoliosis patients, the CoG and LoG are deviated depending on the configuration of the spine. This level of deviation can be roughly understood by measuring the coronal balance, sagittal balance, thoracic trunk shift, thoracolumbar and lumbar sagittal alignment.

A study done by Damavandi et al., [1] on the head and trunk mass, and center of mass position estimations in able-bodied and scoliotic girls concluded that the pre-operative scoliotic girls have greater pelvic forward tilt and trunk inclination compared to normal subjects. Whereas, another study done by Park et al., [2] on the effect of scoliosis angle on sway on the center of gravity found that the whole-body balancing ability in pre-operative scoliosis patients is significantly different from normal persons. This explains the importance of pelvic tilt, the center of gravity, and trunk inclination in maintaining a proper posture. In scoliosis patients, since the trunk posture is altered or shifted to one side, it in turn provides more pressure to the lumbar region on the side of the scoliosis curve. Using image processing, a study conducted by Hajizadeh et al., [3] on a 3D multibody model of the scoliotic spine with lateral bending motion for comparison of ribcage flexibility concluded that the load at lumbar joints in the scoliosis model were higher when compared to the normal subjects. The vertebral column is connected with the pelvis and lower limbs forming a continuous plane for weight transmission and support for the body in bipedal gait and posture of humans. The pelvis is made up

of the hip bones and sacrum. The femur bone of the thigh forms an articulation with the acetabulum to form the hip joint. Weight from the head, arm, and trunk are passed through the vertebral column and transferred to the lower limbs through the sacrum and sacroiliac joint as shown in Figure 1. Intervertebral discs play a major role in transferring load from one vertebra to another. It acts as a shock absorber.

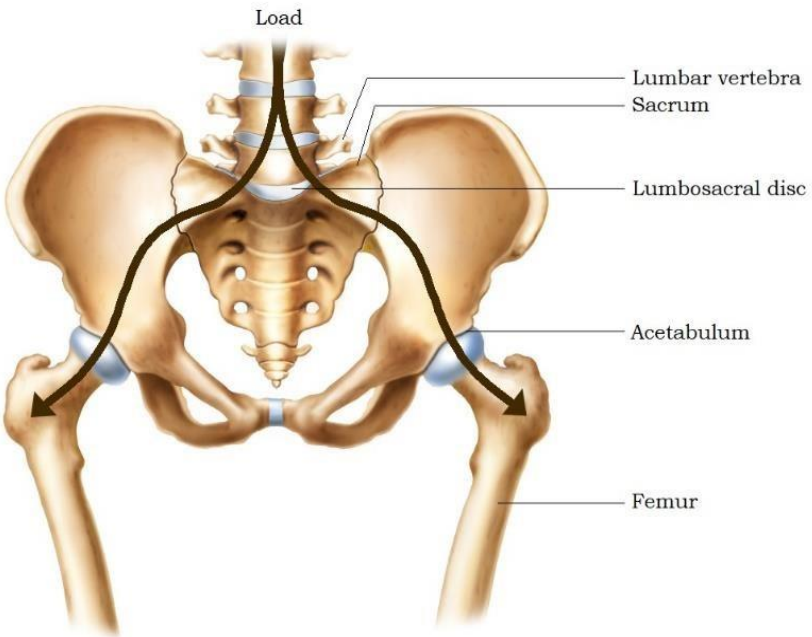

Figure 1: Weight distribution [4].

Pressure within the center of the disc is never zero, because of the pre-existing tension even when the disc is unloaded. The physical property of the intervertebral disc allows it to withstand a considerable amount of load, even when the load is applied for an extended period. A normal intervertebral disc is an anisotropic structure [5]. National Institute for Occupational Safety and Health (NIOSH) guidelines for manual (1994) lifting concluded that the joint between the fifth lumbar vertebra (L_5) and first sacral vertebra (S_1) is the joint of greatest lumbar stress during weight lifting. A study done by Pel et al. found that a 20% reduction in vertical sacroiliac joint shear resulted in a 70% increase in sacroiliac joint compression force [6]. In normal subjects, the vertebral column is arranged linearly in the frontal plane and angular in the sagittal plane. Although, in a scoliotic spine, the vertebral column is

arranged angularly in all three planes as it is often accompanied by some amount of lateral twist in the spine (kyphosis). When scoliosis patients undergo corrective surgery, surgeons focus on correcting the vertebrae causing a scoliosis curve. Surgeons first perform osteotomy (removal of bone parts) and realign the vertebral column manually along the course of the expected normal vertebral curve. Using implants like Harrington rods and Pedicle screws which are made up of stainless steel or titanium, surgeons screw the vertebrae to the Harrington rods using Pedicle screws. Implants are to fix the corrected vertebra in its anatomical position and prevent it from scoliotic recurrence. After fixing the vertebrae, a layer of bone cement or local bone graft is applied over the rearranged vertebral column to fuse the corrected scoliotic vertebrae and to form a single fused vertebra. Thus, the scoliotic vertebral column is rearranged to a new or a normal position.

Some claim that most of the curve is reduced because of the manual pressure. On the other hand, some claim it's due to vertebral fusion and metal implants. A study done by Trobisch et al., [7] on postoperative trunk shift in Lenke 1 and 2 curves concluded that the postoperative trunk shift is common after surgery for adolescent idiopathic scoliosis. But it occurs only in 13.6% of patients and 65% of trunk shifts are iatrogenic (caused by the surgeon). If the curve is corrected only by manual pressure, implants can take over the vertebral fusion. Then need for fusing the vertebrae will be a questionable debate. Even after spinal instrumentation, due to the sudden change in the configuration of the spinal column, patients feel a disturbance in their balance. A study by Carvalho de Abreu et al., [8] on the influence of surgical treatment of adolescent idiopathic scoliosis on postural control supports this theory. They concluded that the scoliosis patients have a large CoP oscillation compared to age-matched healthy adults. Even after surgery, oscillation is decreased in the initial 90 days. But later, it remained larger than before surgery. Also, another study done by Nohara et al., [9] on lumbar disc degeneration in patients with adolescent idiopathic scoliosis with spinal fusion claims that 48% of disc degeneration occurs at the Lumbosacral junction (L_5-S_1) and segments adjacent to fused vertebrae has only 8% of chance. If the abnormal curve (scoliosis) leads to an altered coronal balance, sagittal balance, thoracic trunk shift, thoracolumbar and lumbar sagittal alignment, then after treating scoliosis, these parameters should, by the right return to normal or at least close to normal. This raises a query of whether scoliotic vertebral fusion also affects the non-scoliotic

vertebrae (vertebrae not involved in the scoliotic curve) of the spine. Hence, in order to validate this, this study tried to find the total deformation and strain of the lumbosacral intervertebral disc between the pre and post-operated thoracic scoliosis patients. The objectives of this study were to find whether the manual correction during corrective surgery bring any immediate changes to the structure of the spine and to find whether the correction in the alignment of the thoracic scoliotic spine brings any changes to the biomechanical functionality and load-bearing capacity of the lumbosacral intervertebral disc before and after surgery.

2.0 METHODOLOGY

The prevalent of scoliosis is 1 to 2% in adolescence. Among those 1 to 2%, determining the patients with the same side and the same level of scoliosis who underwent corrective surgery is tiresome work and the availability of such kind of data is exceptional. Hence, this study was an observational cross-sectional study. The sampling method followed was convenience sampling.

2.1 Data Collection

Data collection was done at Government General Hospital, Chennai, India. Proper consent was obtained from the radiology department before collecting data. Since bone fusion gets complete by 6 to 9 months after surgery [10] [11], pre-operative and post-operative CT scan data of patients who underwent scoliosis correction not more than 2 months and with the age group between 10 to 20 years were selected for this study. Only 1 patient fulfilled the above-mentioned criteria. The patient had right thoracic scoliosis and his lumbar bones had normal vertebral alignment. Radiographs were taken with the patient in a lying position. During standing, patients might tilt their pelvis unknowingly. Both the Pre-operative and post-operative radiographs were obtained in DICOM format. Baseline assessments like age, sex, date of surgery, and date of the scan were noted and presented in Table 1.

Table 1: Patient Details

Gender	Age	Pre-operative Scan	Date of Surgery	Post-operative Scan
M	19	12-01-2016	19-01-2016	26-02-2016

2.2 Method

Obtained DICOM files were imported into an image segmentation software Materialise, version 20.0 (Materialise Inc., Belgium). The

lumbosacral joint was selected as the region of interest, which consists of the fifth lumbar vertebra (L_5), sacrum, and lumbosacral disc. Other parts were cropped out. No metal implants, blood vessels, ligaments, endplates, and muscles were comprised in the image segmentation. Two separate masks were created for bones and discs and were converted into parts. The developed parts were smoothened and wrapped to hide any edges or holes. In order to maintain surface contours, an adaptive remesh was carried out with a triangle edge length of 1 mm. Then, the developed parts were converted into solid volume. This solid volume was meshed with 4 node tetrahedral elements and a maximum edge length of 2 mm, to have a uniformed mesh as shown in Figure 2. The meshed volume of the homogeneous lumbosacral segment was exported to an FEA solver program ANSYS, version 17.2 (Ansys, Inc., U.S.A) as .CDB files. The same procedures were followed for both the pre and post-operative DICOM sets.

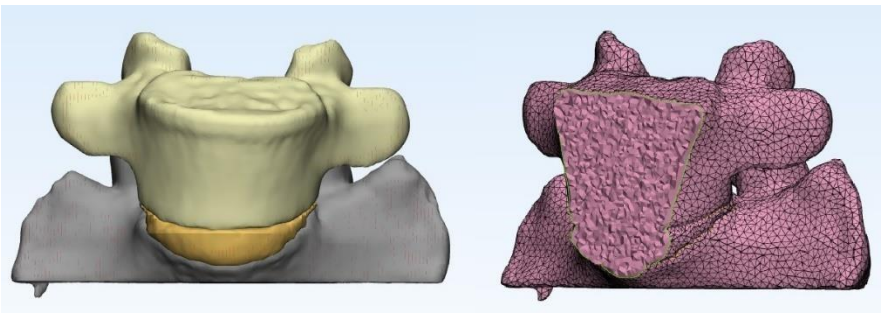

Figure 2: Meshed Lumbosacral Joint

The exported .CDB files were opened with the Ansys Workbench module. Static structural analysis was set to run. A linear homogeneous isotropic material property was used to run the simulation. The isotropic material properties of bone and disc were attained from works of literature [12] and [13] and provided in Table 2. The large deflection was turned off and the direct solver type was selected. In our previous study [14], it was found that on a normal standing position, an average adult weighing 65 kgs with a normal lumbosacral angle of 30° would exert a net force of 196 N on the lumbosacral disc. Hence, the same 196 N force was applied in this model. The sacrum was set as fixed support and 196 N downward force was applied on the L_5 vertebra. The total deformation and equivalent elastic strain of the lumbosacral disc were measured.

Table 2: Material properties of Homogeneous model

	Young's Modulus (MPa)	Poisson's Ratio	References

Bone	200	0.3	[12, 13]
Disc	4	0.4999	

3.0 RESULTS AND DISCUSSION

Results of applying 196 N force on the lumbosacral disc between pre and post-operative models showed us that there is a difference between them. Before the correction, the total deformation and equivalent elastic strain of the lumbosacral disc were found to be 0.00020242 m and 0.03153 m/m. Whereas, after correction and before complete fusion of the scoliotic vertebrae, the total deformation and equivalent elastic strain of the lumbosacral disc was found to be 0.00011567 m and 0.019186 m/m. The number of nodes, elements, total deformation, and equivalent elastic strain of pre-operative and post-operative models is represented in Table 3.

Table 3: Results. TD – Total Deformation, EES – Equivalent Elastic Strain

	Pre-operative	Post-operative
Nodes	65755	58247
Elements	385584	326962
TD	0.00020242 m	0.00011567 m
EES	0.03153 m/m	0.019186 m/m

It was evident that the area of total deformation and area of equivalent elastic strain in pre and post-operative discs had changed. In the pre-operative lumbosacral disc, the maximum area of total deformation was on the anterior aspect of the disc. Much force was concentrated on the anterior and had uneven distribution. Whereas, in post-operative, the maximum area of total deformation was on the anterolateral aspect of the disc and the force of 196 N was distributed to the disc to a certain extent as shown in Figure 3.

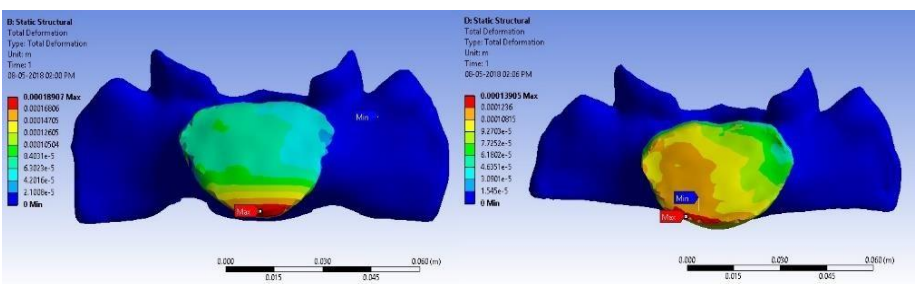

(a) (b)

Figure 3: Total Deformation of Lumbosacral disc; (a) Pre-operative and

(b) Post-operative

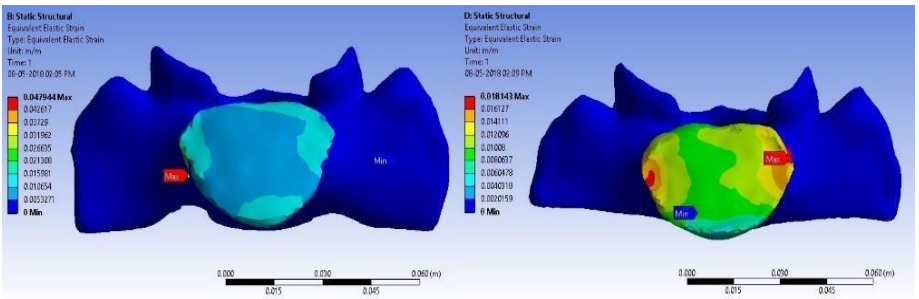

(a) (b)

Figure 4: Equivalent Elastic Strain of Lumbosacral disc; (a) Pre-operative and (b) Post-operative

We noticed the same level of changes in the equivalent elastic strain as well. In pre-operative it was found that the maximum strain was on the lateral aspect of the disc (right side). In post-operative, the maximum strain was found nearly on both the sides (lateral) on top (superior) of the disc as shown in Figure 4. It is also important to note that the number of nodes and elements of the same patient varies between pre and post-operated lumbosacral models.

Earlier, a study by Karami et al., [15] on the assessment of coronal radiographic parameters of the spine in the treatment of adolescent idiopathic scoliosis concluded that precise attention to the coronal balance in pre-operative is vital in the prevention of post-operative decompensation. During the scoliosis correction surgery, surgeons perform osteotomy, place bone grafts in the course of the scoliosis curve, and fuse the vertebrae together. With the help of metal implants, bone grafts, and bone regeneration, curve correction occurs promptly. Another study by Ameri et al., [16] on the natural history of coronal balance after spinal fusion in adolescent idiopathic scoliosis revealed that the first 12 months after posterior spinal fusion is the spontaneous improvement period for coronal balance.

Our earlier study [17] on thoracic trunk shift and coronal balance conducted among 24 pre and post-operated thoracic scoliosis patients found that there is a significant decrease in the trunk shift and coronal balance between pre and post-operative patients. These 24 thoracic scoliosis patients are those who underwent correction surgery at least a year before the date of data collection. Their X-Ray images were used for measurement. The pre-operative thoracic trunk shift and coronal

balance were measured to be 42.45 ±10.36 mm and 14.75 ±4.12 mm. Whereas, the post-operated thoracic trunk shift and coronal balance were measured to be 14.83 ±5.18 mm and 4.25 ±1.35 mm. Since the patients had 12 months of duration from the date of surgery to the date of data collection, this decrease in trunk shift and coronal balance could be because of the implants and vertebral bone fusion. Whereas, the present study was conducted with the patient who had only a 1-month duration between the date of surgery and the date of data collection. This indicates that, along with the implants and vertebral bone fusion, the surgeon's manual correction of scoliotic vertebral alignment also plays a major role in scoliosis correction. After correction, the vertebral column gets a new alignment. This forces the rest of the adjacent vertebrae and other bones like ribs and sacrum to regenerate accordingly. This regeneration of bones after scoliosis correction could be the reason for the difference in the number of nodes and elements between the pre and post-operated lumbosacral model of the same patient.

This study had few limitations. Human bone is nonhomogeneous and anisotropic. Since the volume of the lumbosacral segment is small and this study aimed to find only the structural change between pre and post-operative, the property of bone and disc were assumed to be homogeneous and isotropic. The second limitation was the mesh independence study. Instead of performing a mesh independence study to find the optimal mesh size, a standard mesh size of 2 mm was selected as it was widely used in the literature. It is advisable that the upcoming researchers use more sample size, perform mesh independence study, and consider the model as nonhomogeneous and anisotropic to get more precise results.

4.0 CONCLUSION

This study results showed that, the total deformation and equivalent elastic strain of lumbosacral disc at 196 N force as 0.00020242 m and 0.03153 m/m. Whereas, after correction and before complete fusion of the scoliotic vertebrae, it was found to be 0.00011567 m and 0.019186 m/m. From this study, it can also be inferred that manual correction in the alignment of the thoracic scoliotic spine during corrective surgery brings immediate changes to the structure of the spine, changes in the disc load distribution pattern, and bone remodeling in the adjacent vertebrae, ribs, and sacrum. This helps in the improvement of the functional capacity of the individual and thus helps in reducing the morbidity due to the deformity before correctional surgery.

5.0 ACKNOWLEDGMENTS

A heartfelt thanks to Dr. Nalli R Yuvaraj, orthopedic spine surgeon from Rajiv Gandhi Government General Hospital, Chennai, for his help and constant support during the data collection. Cordial thanks to Dr. Chin Seong Lim, Faculty of Engineering, University of Nottingham Malaysia, for his help and support in performing structural simulations at the University of Nottingham Malaysia.

6.0 REFERENCES

[1] M. Damavandi, G. Dalleau, G. Stylianides, C.-H. Rivard and P. Allard, "Head and Trunk mass and center of mass position estimates in able-bodied and scoliotic girls," *Medical Engineering & Physics,* vol. 35, no. 11, pp. 1607-1612, 2013. DOI: 10.1016/j.medengphy.2013.05.010

[2] J.-Y. Park, G. D. Park, S.-G. Lee and J.-C. Lee, "The Effect of Scoliosis Angle on Center of Gravity Sway," *Journal of Physical Therapy Science,* vol. 25, no. 12, pp. 1629-1631, 2013. DOI: 10.1589/jpts.25.1629

[3] K. Hajizadeh, I. Gibson and L. G, "Developing a 3D Multi-Body Model of the Scoliotic Spine with Lateral Bending Motion for Comparison of Ribcage Flexibility," *International Journal of Advanced Design and Manufacturing Technology,* vol. 6, no. 1, pp. 25-32, 2013. URL: http://admt.iaumajlesi.ac.ir/article_534824.html

[4] Dr. Morris. (2015). *Pelvic Discomfort in Pregnancy* [Online]. Available: http://www.drmorris.com.au/pelvic-discomfort-in-pregnancy/. [Accessed 12 May 2021].

[5] X. Gao, Q. Zhu and W. Gu, "An Anisotropic Multiphysics Model for Intervertebral Disk," *Journal of Applied Mechanics,* vol. 83, no. 2, pp. 11-18, 2016. DOI: 10.1115/1.4031793

[6] J. J. Pel, C. Spoor, A. Pool-Goudzwaard, G. Hoek van Dijke and C. Snijders, "Biomechanical Analysis of Reducing Sacroiliac Joint Shear Load by Optimization of Pelvic Muscle and Ligament Forces," *Annals of Biomedical Engineering,* vol. 36, no. 3, pp. 415-424, 2008. DOI: 10.1007/s10439-007-9385-8

[7] P. D. Trobisch, A. F. Samdani, J. Pahys and P. J. Cahill, "Postoperative trunk shift in Lenke 1 and 2 curves: how common is it? and analysis of risk factors," *European Spine Journal,* vol. 20, no. 7, pp. 1137-1140, 2011. DOI: 10.1007/s00586-011-1820-8

[8] D. C. Carvalho de Abreu, M. M. Gomes, H. A. Rocha de Santiago, C. F. P. d. S. Herrero, M. A. Porto and H. L. Aparecido Defino, "What is the influence of surgical treatment of adolescent idiopathic scoliosis on postural control?," *Gait Posture,* vol. 36, no. 3, pp. 586-590, 2012. DOI: 10.1016/j.gaitpost.2012.05.019

[9] A. Nohara, N. Kawakami, K. Seki, T. Tsuji, T. Ohara, T. Saito and K. Kawakami, "The Effects of Spinal Fusion on Lumbar Disc Degeneration in Patients with Adolescent Idiopathic Scoliosis: A Minimum 10-Year Follow-Up," *Spine Deformity*, vol. 3, no. 5, pp. 462-468, 2015. DOI: 10.1016/j.jspd.2015.04.001

[10] E. M. Mannen and D. E. Anderson, "Mechanical testing of the thoracic spine and related implants," in *Mechanical Testing of Orthopaedic Implants*, Duxford, Woodhead Publishing, 2017, pp. 143-160. DOI: 10.1016/B978-0-08-100286-5.00008-1

[11] T. Shimizu, L. G. Kenke, M. Cerpa, E. Beauchamp, L. Y. Carreon, C. I. Shaffrey, K. M. Cheung and M. G. Fehlings, "A Radiographic Analysis of Lumbar Fusion Status and Instrumentation Failure After Complex Adult Spinal Deformity Surgery With Spinopelvic Fixation: Two-Year Follow-up From the Scoli-Risk-1 Prospective Database," *Clinical Spine Surgery*, vol. 33, no. 10, pp. 545-552, 2020. DOI: 10.1097/BSD.0000000000001008

[12] H. Li and Z. Wang, "Intervertebral disc biomechanical analysis using the finite element modeling based on medical images," *Computerized Medical Imaging and Graphics*, vol. 30, no. 6-7, pp. 363-370, 2006. DOI: 10.1016/j.compmedimag.2006.09.004

[13] N. Homma, *An Approach to Lumbar Vertebra Biomechanical Analysis Using the Finite Element Modeling Based on CT Images*, Rijeka: InTech, 2011. URL: https://downloadmedicalbooks.files.wordpress.com/2011/08/theory_and_applications_of_ct_imaging_and_analysis.pdf

[14] M. Palaniswamy, W. Y. Leong, K. H. Cheah and L. C. Yong, "Engineering concepts in analysing lumbosacral load in post-operative scoliotic patients," *Journal of Engineering Science and Technology*, vol. 13, no. 4, pp. 1058-1069, 2018. URL: http://jestec.taylors.edu.my/Vol%2013%20issue%204%20April%202018/13_4_15.pdf

[15] M. Karami, A. Maleki and K. Mazda, "Assessment of Coronal Radiographic Parameters of the Spine in the Treatment of Adolescent Idiopathic Scoliosis," *The Archives of Bone and Joint Surgery*, vol. 4, no. 4, pp. 376-380, 2016. DOI: 10.22038/abjs.2016.7538

[16] E. Ameri, H. Ghandhari, N. Nabizadeh and H. Hesarikia, "Natural history of coronal balance after spinal fusion in adolescent idiopathic scoliosis," *Journal of Research in Orthopedic Science*, vol. 1, no. 2, 2014. URL: http://jros.iums.ac.ir/article-1-117-en.html

[17] M. Palaniswamy and W. Y. Leong, "Evaluation on Thoracic Trunk Shift and Coronal balance in Post-Operative Scoliosis Patients," *ASM Science Journal*, vol. 11, no. 1, pp. 1-8, 2018. URL: https://www.akademisains.gov.my/asmsj/article/evaluation-on-

thoracic-trunk-shift-and-coronal-balance-in-post-operative-scoliosis-patients/

APPLICATION OF DIGITAL SIGNAL PROCESSING AND MACHINE LEARNING FOR ELECTROMYOGRAPHY: A REVIEW

S.N. Omar[1], N.M. Saad[1,*], A.R. Abdullah[2], E.F. Shair[2] and T.N.S.T. Zawawi[2]

[1]Faculty of Electrical and Electronic Engineering Technology.
[2]Faculty of Electrical Engineering.
Universiti Teknikal Malaysia Melaka, Durian Tunggal, 76100, Melaka, Malaysia

[*]Corresponding Author's Email: [1]norhashimah@utem.edu.my

Article History: Received June 7, 2021; Revised July 9, 2021; Accepted July 16, 2021

ABSTRACT: Digital signal processing (DSP) and Machine learning (ML) have emerged as promising approaches to automate prediction tasks into electromyography (EMG) muscles conditions. To fill the research gap, This paper reviews the state-of-the-art applications of DSP and ML for EMG signal analysis. DSP techniques to extract information of EMG signal is highly needed. The major disadvantage of the frequency domain approach is it does not represent temporal information. Many time-frequency analysis techniques have been proposed. However, there is a compromise between time and frequency resolution. The techniques that minimize the EMG noise and analyze signal characteristics are discussed together to identify the best performance with the highest percentage of accuracy and efficiency. The most appropriate method depends on the EMG signal patterns, the quality and quantity of the signals and training data developed, and various types of user factors.

***KEYWORDS**: Digital Signal Processing; Machine Learning; Electromyography*

1.0 INTRODUCTION

The work on electromyography (EMG) signal processing, as well as the utilization of EMG signal analysis for clinical applications and engineering studies such as prosthetic arms and musculoskeletal disorders, will be discussed in this presentation. The basic theory of myoelectric signal creation will be briefly discussed at the outset of this

study [1]. Following that, the signal processing techniques used on the EMG signal such as time domain, frequency domain, and the time-frequency domain will be discussed [2].

It includes signal acquisition methods, such as noise removal, as well as signal processing techniques such as amplitude and spectrum analysis. This paper will also look at several works and works of literature on the use of the EMG signal as a tool for various applications such as clinical diagnosis, motion analysis, prosthetic device, and to know the performance of the muscles [3].

Machine learning algorithms, such as traditional machine learning algorithms, and reinforcement learning algorithms, have been widely used in the medical field and have played an important role in the diagnosis and treatment of diseases as an essential component of artificial intelligence [4].

Thus, in this paper, some types of DSP methods and machine learning will be discussed to identify the proper and optimum method that can provide more information from the signal characteristics and the ML to identify the type of algorithm that can give the highest performance comparisons of accuracy.

2.0 THE RELATION OF DIGITAL SIGNAL PROCESSING, MACHINE LEARNING AND ELECTROMYOGRAPHY

2.1 Electromyography (EMG)

Electromyography (EMG) is the measurement of electrical potential arising from electrochemical effects due to muscle contractions. These signals are transmitted via human tissue to the surface of the skin, where they can be measured by surface EMG electrodes and it is a complicated and non-stationary signal, which is controlled by the human nervous system. Areas of application for these sensors include exoskeletons, diagnostics, and myoelectric hand prostheses [5]–[7]. EMG has become a reliable and cost-effective method for signal acquisition in limbs. Placing electrodes inappropriate position of skin is an important criterion to get the optimum EMG signals [8], [9].

2.1.1 EMG Signal Analysis

The EMG signal is a biomedical signal that measures electrical currents generated in muscles during their contraction representing neuromuscular activities. The nervous system continuously controls muscle activity such as during contraction and relaxation. EMG signal is a complex signal, which is controlled by the nervous system and is

dependent on the anatomical and physiological properties of muscles. EMG signal acquires noise while travelling via different tissues [10]. This signal is a complex and non-stationary signal, which is controlled by the human nervous system. The amplitude of EMG signals is a very small value between 50uV to 1mV, with the frequencies varying from 10 Hz to 3000 Hz [11]. The EMG signals can be measured by applying electrodes to the skin surface (non-invasive method) or intramuscular (invasive method) within the muscle. Even though the efficiency of surface EMG is lower than the intramuscular EMG, but still for research purposes, surface EMG is more popular since it is non-invasive and more convenient to use [12]. Figure 1 shows the EMG signal for normal muscle during contraction.

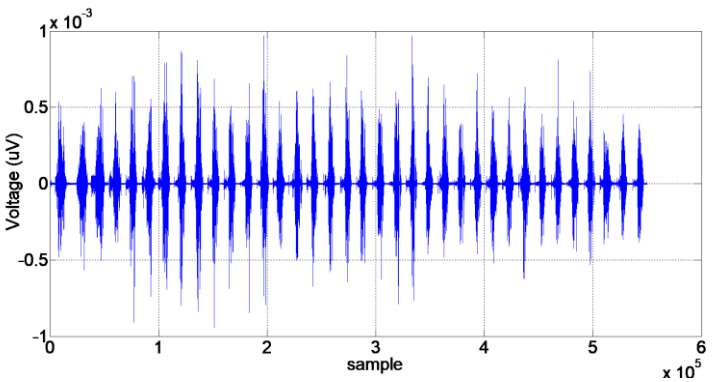

Figure 1: Normal EMG Signal

The flow of EMG signal analysis is divided into some phases for the health screening task. Figure 2 shows the flow phase of EMG signal analysis. There are four phases which are raw data collection of EMG signal, pre-processing, analysis of features extraction and classification of EMG signal by using time-frequency distribution (TFD) and signal classification.

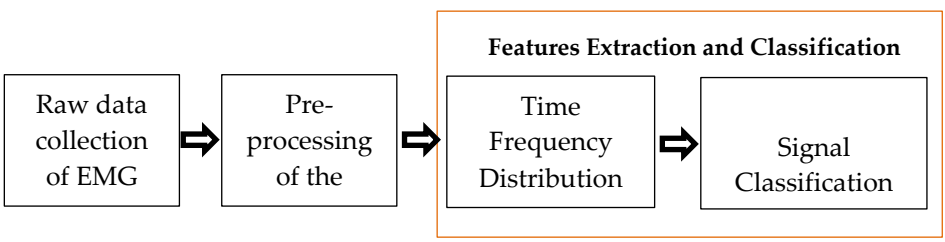

Figure 2: Flow phase of EMG signal analysis

It has been commonly accepted that the preferred manner for

processing the EMG signal is to calculate the integrated rectified signal. This was done by rectifying (rendering the signal to have excursions of one polarity) the EMG signal, integrating the signal over a specified interval of time, and subsequently forming a time series of the integrated values. The advances made in electronics devices during the past decades have made it possible to conveniently and accurately calculate the root-mean-squared (RMS) and the average rectified (AVR) value of the EMG signal. The AVR value is similar to the integrated rectified value if the calculations are made correctly and accurately.

Both these variables provide a measurement of the area under the signal but do not have a specific physical meaning. The EMG signals which are going to be analyzed are represented in time-frequency representation (TFR) which includes parameters such as instantaneous RMS voltage. Frequency domain analysis that the first frequency analysis technique used is known as the Fast-Fourier Transform (FFT).

FFT is the mathematical technique to convert the signal from a time domain to a frequency domain. FFT is performed to estimate the frequency characteristics of the EMG signal. The limitation of the FFT is that it is not able to cater to non-stationary signals whose spectral characteristic changes in time. This can be overcome by the Linear Time-Frequency distribution (TFD) technique.

To increase the test efficiency of patients' muscle condition a technique to extract information is highly needed. Many time-frequency analysis techniques have been proposed and one of the most commonly used is short-time Fourier transform (STFT) which is a form of linear time-frequency distribution (TFD) [13]. However, the major disadvantage is that it does not represent temporal information. [12]. To solve the problem, Dennis Gabor (1946) improved the Fourier analysis to small sections of signals and divided by the time of analysis in intervals.[14]. The main shortcoming of this method is that there is a compromise between time and frequency resolution. The main disadvantage of this technique is that there is a compromise between time and frequency resolution. The greater the temporal resolution required, the worse the frequency resolution will be and vice versa. Figure 3 shows the example of the time-frequency representation (TFR) of a signal using the STFT. The TFR presents the temporal and spectral information of the signal [15].

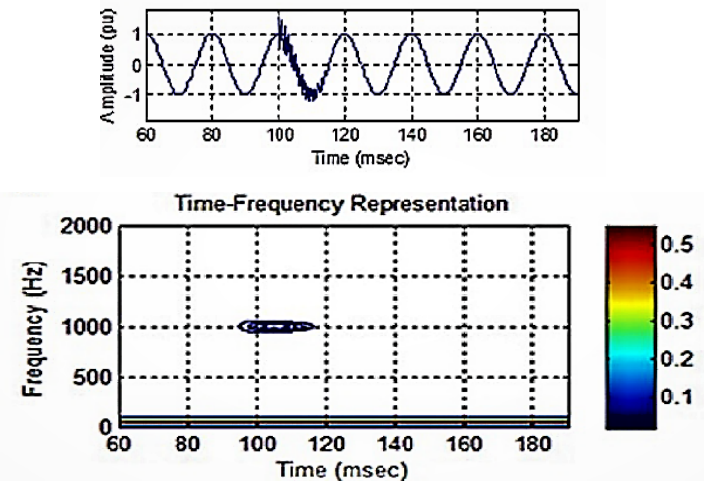

Figure 3: Example of time-frequency representation using Short Time Fourier Transform (STFT) [15]

2.1.2 Equipment for Data Collection EMG signal

Consensys is the software that works together with Shimmer sensors which adds significant features to live data, managed data, and devices. It is adaptive human data collection in the field, large-scale repeatable trials, and general multi-sensor management. Consensys enables the following functionalities as Configuring Shimmer sensors, Streaming real-time data, and Managing collected data. Figure 4 (a)(b)(c) shows the Consensys software Interface [16].

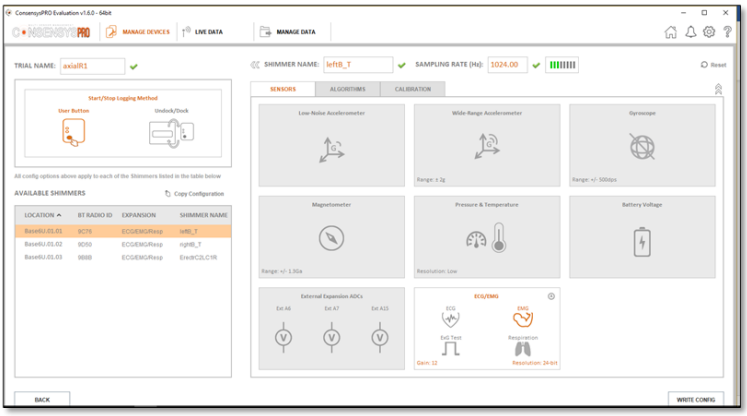

Figure 4: Consensys software Interface [16]

The Shimmer3 Consensys EMG Development Kit can be utilized to monitor two channels of non-invasive surface EMG, providing a representation of the muscle activity at the measurement site. The EMG Development Kit can also be utilized to monitor ECG (Electrocardiogram), recording the pathway of electrical impulses through the heart muscle. Combined with Shimmer's integrated altimeter and 9DoF inertial sensor platform, greater context can be given to the wearer's activity and condition in real-time. Figure 5 shows the Consensys EMG Development Kits [17].

Figure 5: Consensys EMG Development Kits

The Shimmer3 EMG unit can measure and records the electrical activity associated with muscle contractions, assesses nerve conduction, muscle response in injured tissue, activation level, or can

be used to analyze and measure the biomechanics of human or animal movement. Other than that, it can provide a configurable digital front-end, optimized for the measurement of physiological signals for EMG[18].Shimmer3 EMG sensor consists of two channels of EMG data as shown in Figure 6 and EMG data can be measured simultaneously with 10DOF kinematic data.

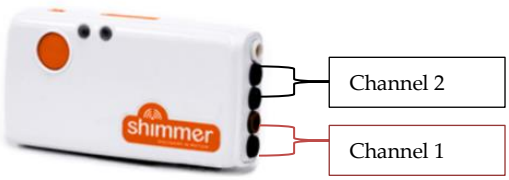

Figure 6: Consensus Shimmer3 EMG Unit

Consensys Base6 (Figure 7) is used to configure and capture data from multiple sensors simultaneously, to simplify the setup of trials and storage of recorded data. The key features of Consensys Base6 consist of Shimmer3 firmware updating, Shimmer configuration, Multi-Shimmer synchronization, and logged data management [19]. Other than that, the functional Base6 is to provide for the simultaneous management of all your Shimmer Sensors including charging, firmware updates, configuring sensors, retrieving and processing logged data. Besides that, Consensys Base6 is compatible with the Shimmer3 range of Kinematic and Biophysical sensors including ECG, EMG, Galvanic Skin Response, Optical Pulse, and Heart Rate as shown in Figure 8.

Figure 7: Consensus Shimmer Base6

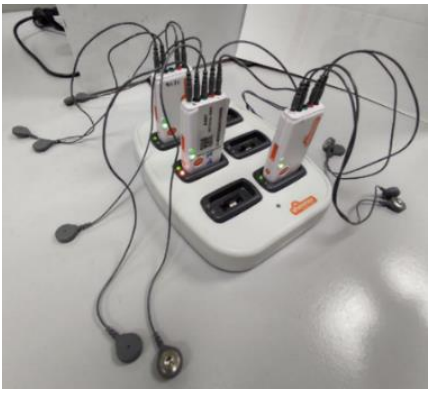

Figure 8: Installation Consensus Shimmer3 EMG Unit on Base6

The Shimmer MATLAB is the Instrument Driver which is an orientated solution for Shimmer to capture the data directly into MATLAB. This driver will allow Shimmer users to stream data directly to MATLAB, and assist users of the Shimmer3 Platform in the development of Shimmer-based applications in MATLAB. Figure 9 shows the interface of the Shimmer MATLAB Instrument Driver [20].

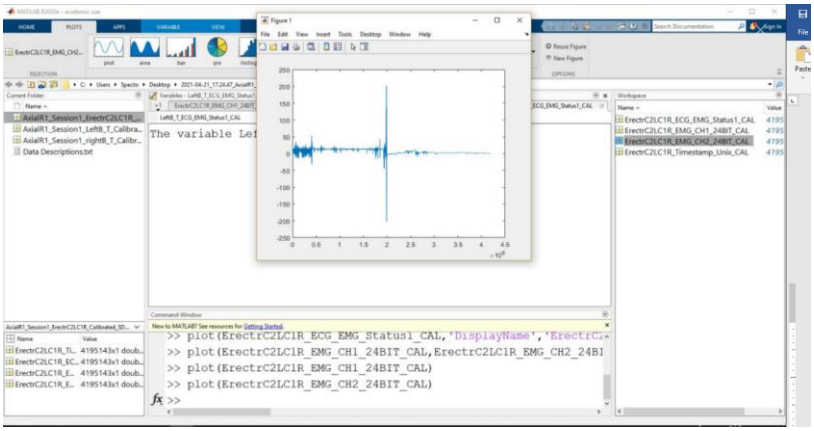

Figure 9: Shimmer MATLAB Instrument Driver [20]

2.2 Digital Signal Processing (DSP)

Digital signal processing is known as one of the elementary technologies utilized in the field of biomedical engineering [21] other than communication [22]–[24]. Digital signal processing is the method to process signals by using numerical methods. It is a subject that uses computers or special digital processing equipment. The typical

purpose of digital signal processing is the acquisition of biological signal, noise reduction, signal transformation, analysis, synthesis, filtering, evaluation, identification, and others so that the required signal can be extracted [1],[25]. The basic flow of the digital signal processing is shown in Figure 10.

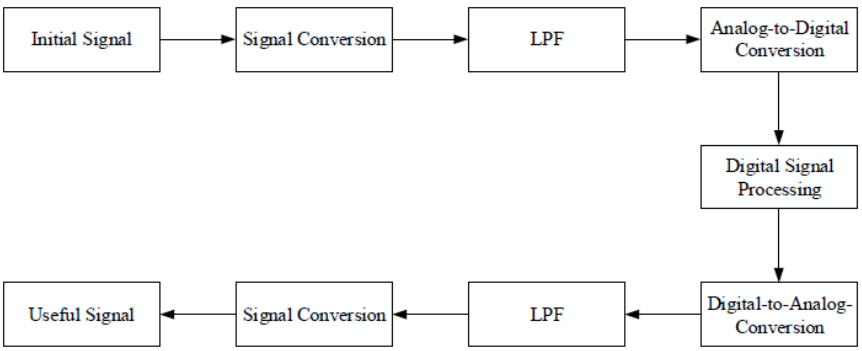

Figure 10: Digital Signal Processing Flow [22]

Digital signal processor that can execute different things, depending on the application being performed. Some of these variants are audio signal processing, audio and video compression, speech processing and recognition, digital image processing, and radar applications. The difference between each of these applications is how the digital signal processor can filter each input. Five different aspects vary from each DSP: clock frequency, RAM size, data bus width, ROM size, and I/O voltage [26].

2.3 Machine Learning (ML)

Machine learning is one of the artificial intelligence (AI) that predicts the outcome without relying upon the pre-determined equation. Machine learning learns the information directly from the data and it instructs the computer to do by learning from the experience [17]. Machine learning is divided into supervised and unsupervised learning. More specifically, classification is one type of supervised learning. Unlike unsupervised learning, supervised learning predicts the categorical responses from known response data set [18]. Moreover, machine learning is learned from experience, which is the features extracted from the signals. In recent days, the classifiers such as support vector machines (SVM), k-nearest neighbour (k-NN), linear discriminate analysis (LDA), naïve Bayes (NB), artificial neural network (ANN), general regression neural network (GRNN), multilayer perceptron neural network (MLPNN) and decision tree (DT) are widely used in the

classification of EMG signals.

Machine learning represents an effective method for data analysis in many domains: it has recently demonstrated its effectiveness in processing tactile sensor data [27]. Machine learning and artificial intelligence applications have grown rapidly across several disciplines, industries, and cultures.[28]–[30].

3.0 APPLICATION OF DIGITAL SIGNAL PROCESSING AND MACHINE LEARNING FOR EMG

In 2016 Elhan Umut and Güven Çentik has been studies the Digital Signal Processing in EMG [31] .In this study, the researcher intended to detect periodic leg movement (PLM) in sleep with the use of the channels except for leg electromyography (EMG) by analyzing polysomnography (PSG) data with digital signal processing (DSP) and machine learning methods. PSG records of 153 patients of different ages and genders with PLM disorder diagnoses were examined retrospectively. A novel software was developed for the analysis of PSG records. The software utilizes machine learning algorithms, statistical methods, and DSP methods. To classify PLM, popular machine learning methods (multilayer perceptron, *K*-nearest neighbour, and random forests) and logistic regression were used.

Next, in the same year in 2016, Theresa Roland and his teams used the same application regarding DSP and EMG [32]. The teams introduced the new capacitive measurement system to the application in prostheses. A capacitive EMG prototype, consisting of a flexible sensor and measurement electronics, was developed. The electronic circuit, used for signal amplification and filtering, is described. An ultralow-power microcontroller was used for the implementation of algorithms for EMG signal processing. DSP algorithms were optimized for real-time processing and minimal computing power. Muscle signals, measured with this prototype, are presented.

In the year 2021, Basilio Vescio has developed and validated a new mobile tool for the automated and quantitative characterization of phase displacement resting tremor pattern in ambulatory clinical settings using DSP for μEMG application [33]. A new low-cost, wearable mobile device, called, μEMG, is described, based on low-end instrumentation amplifiers and simple digital signal processing (DSP) capabilities.

3.1 Machine Learning in EMG

Back in 2017, a study has been done by Jianyun that involves ML in EMG studies [34]. In his study, the real-time TMS320C6748 DSP was used instead of Matlab to collect and analyze the surface electromyography (SEMG), to realize the real-time detection of electromyogram (EMG) parameters. He uses the frequency domain feature extraction method to analyze muscle fatigue, and study the effectiveness of the EMG fatigue analysis.

For two years, Jianhua Zhang and his team have developed extracted four time-domain features of the EMG signals and use a generative graphical model, Deep Belief Network (DBN), to classify the EMG signals [35]. A DBN is a fast, greedy deep learning algorithm that can rapidly find a set of optimal weights of a deep network with many hidden layers.

In 2020, similar technologies in ML and EMG have been used in studies done by Yuri Kovalev and JoyRoy [36], [37]. Yuri has created a system for controlling devices using EMG signals from a small number of sensors by recognizing signal sections corresponding to the operator's gestures. The solution implements a scheme of three independent components: sensors, a user interface, and a data processor, connected by a simple data transfer protocol, which allows replacing any of the parts if necessary.

While Joy Roy investigated the different machine learning techniques for predicting the SEMG activities on upper limb muscles. Various issues were presented for predicting SEMG activities on upper limb muscle including muscle classification techniques, muscle selection, and SEMG parameter to signify the muscle activities. These outcomes can be applied for predicting the upper limb muscle activities to identify the critical situation of neuromuscular disorders patients.

Any brain-computer interface (BCI) system must translate signals from the user's brain into messages or commands [38]. Many signal processing and machine learning techniques have been developed for this signal translation. Although these techniques are often illustrated using electroencephalography (EEG) signals, they are also suitable for other brain signals. Gurjit and his team have proposed a novel combination of supervised ML with DSP, resulting in ML-DSP: an alignment-free software tool for ultrafast, accurate, and scalable genome classification at all taxonomic levels [39]. They test ML-DSP by classifying 7396 full mitochondrial genomes at various taxonomic levels, from kingdom to genus, with an average classification accuracy of less than 97%.

4.0 CONCLUSION

From this study, it has been founded that the application of DSP and ML in EMG is widely used through various technologies and implementations. All the studies revealed that DSP and ML are related to each other wherein biosignal processing there is a need of the DSP and ML application into the EMG study to classify the signal to minimize the EMG noise of signal, However, most of the studies do not cover the EMG study using ML and DSP altogether. They only managed to focus on certain areas and segments that are related to the field of their study. Thus, this paper will help the future researcher to find the information on the relationship between EMG, digital signal processing as the technique of signal analysis, and machine learning for classification method to provide the best method and classification for EMG signal or another clinical nerve electrophysiology including electroencephalography (EEG).

5.0 ACKNOWLEDGMENTS

The authors would like to thanks the Universiti Teknikal Malaysia Melaka (UTeM), Faculty of Electrical and Electronic Engineering Technology (FTKEE) and Faculty of Electrical Engineering (FKE), Advance Digital Signal Processing (ADSP) Lab, Centre of Robotic and Industrial Automation (CeRIA) and Ministry of Higher Education (MOHE), Malaysia that supported this research under project FRGS/1/2020/FTKEE CERIA/F00428.

6.0 REFERENCES

[1] A. K. Mukhopadhyay and S. Samui, "An experimental study on upper limb position invariant EMG signal classification based on deep neural network," *Biomed. Signal Process. Control*, vol. 55, p. 101669, Jan. 2020.

[2] A. Phinyomark, R. N. Khushaba, and E. Scheme, "Feature extraction and selection for myoelectric control based on wearable EMG sensors," *Sensors (Switzerland)*, vol. 18, no. 5, pp. 1–17, 2018.

[3] A. Norali and M. Som, "Surface Electromyography Signal Processing and Application: A Review," in *International Conference on Man-Machine Systems*, 2009, no. October, pp. 11–13.

[4] T. Liu, Z. Li, Y. Tang, D. Yang, S. Jin, and J. Guan, "The application of the machine learning method in electromyographic data," *IEEE*

Access, vol. 8, pp. 9196–9208, 2020.

[5] T. Roland, S. Amsuess, M. F. Russold, and W. Baumgartner, "Ultra-low-power digital filtering for insulated EMG sensing," *Sensors (Switzerland)*, vol. 19, no. 4, p. 959, 2019.

[6] M. A. Cavalcanti Garcia and T. M. M. Vieira, "Surface electromyography: Why, when and how to use it," *Rev. Andaluza Med. del Deport.*, vol. 4, no. 1, pp. 17–28, 2011.

[7] "Prosthetics 2017/18, Upper Limb, Otto Bock Healthcare GmbH." https://www.ottobock.se/media/local_media_1/bu-prosthetics/nedladdning/ottobock___prosthetics___ul_catalogue_646k6_gb_04_1709.pdf (accessed May 29, 2021).

[8] K. Samarawickrama, S. Ranasinghe, Y. Wickramasinghe, W. Mallehevidana, V. Marasinghe, and K. Wijesinghe, "Surface EMG Signal Acquisition Analysis and Classification for the Operation of a Prosthetic Limb," *Int. J. Biosci. Biochem. Bioinforma.*, vol. 8, no. 1, pp. 32–41, 2018.

[9] Y. Blanc and U. Dimanico, "Electrode Placement in Surface Electromyography (sEMG) "Minimal Crosstalk Area" (MCA)," *Open Rehabil. J.*, vol. 3, no. 1, pp. 110–126, 2014.

[10] R. H. Chowdhury, M. B. I. Reaz, M. A. Bin Mohd Ali, A. A. A. Bakar, K. Chellappan, and T. G. Chang, "Surface electromyography signal processing and classification techniques," *Sensors (Switzerland)*. 2013.

[11] B. Widanarko *et al.*, "Prevalence and work-related risk factors for reduced activities and absenteeism due to low back symptoms," *Appl. Ergon.*, vol. 43, no. 4, pp. 727–737, Jul. 2012.

[12] A. Costa, M. Itkonen, H. Yamasaki, F. S. Alnajjar, and S. Shimoda, "Importance of muscle selection for EMG signal analysis during upper limb rehabilitation of stroke patients," 2017.

[13] H. Daneshmandi, A. R. Choobineh, H. Ghaem, M. Alhamd, and A. Fakherpour, "The effect of musculoskeletal problems on fatigue and productivity of office personnel: A cross-sectional study," *J. Prev. Med. Hyg.*, vol. 58, no. 3, pp. E252–E258, 2017.

[14] D. Starovoytova, "Hazards and Risks at Rotary Screen Printing (Part 2/6): Analysis of Machine-operators' Posture via Rapid-Upper-Limb-Assessment (RULA)," *Ind. Eng. Lett.*, vol. 7, no. 5, pp. 42–63, 2017.

[15] B. Boashash, *Time-Frequency Signal Analysis and Processing: A Comprehensive Reference*. Oxford, 2003.

[16] "ConsensysPRO Software | Collect and analyze biometric and motion data from Shimmer sensors." https://www.shimmersensing.com/products/consensys.

[17] "Consensys Bundle Development kit | Complete Wearable Sensor Kit | IMU - ECG - EMG - GSR." https://www.shimmersensing.com/products/consensys-ecg-development-kits-update.

[18] "Wearable EMG Sensor | Wireless EMG sensor | Electromyogram." https://www.shimmersensing.com/products/shimmer3-emg-sensor.

[19] "Physiological & kinematic data capture with the Base6 | Multi sensor management | Charging dock." https://www.shimmersensing.com/products/consensys-base6.

[20] "Shimmer MATLAB Instrument Driver - File Exchange - MATLAB Central." https://ww2.mathworks.cn/matlabcentral/fileexchange/43712-shimmer-matlab-instrument-driver.

[21] Y. Ono, "Back to basics series: Digital signal processing," *Trans. Japanese Soc. Med. Biol. Eng.*, vol. 57, no. (2-3), pp. 75–80, 2019.

[22] H. Lu, Y. Xiaoyu, W. Haodong, L. Jin, M. Xuejiao, and Z. Caihong, "Research on Application of Digital Signal Processing Technology in Communication," 2020.

[23] K. Zhong, X. Zhou, J. Huo, C. Yu, C. Lu, and A. P. T. Lau, "Digital Signal Processing for Short-Reach Optical Communications: A Review of Current Technologies and Future Trends," *J. Light. Technol.*, vol. 36, no. 2, pp. 1–24, 2018.

[24] T. Kobayashi, F. Hamaoka, M. Nakamura, H. Yamazaki, M. Nagatani, and Y. Miyamoto, "Ultrahigh-speed optical communications technology combining digital signal processing and circuit technology," *NTT Tech. Rev.*, 2019.

[25] D. Goyal, C. Mongia, and S. Sehgal, "Applications of Digital Signal Processing in Monitoring Machining Processes and Rotary Components: A Review," *IEEE Sensors Journal*, vol. 21, no. 7. 2021.

[26] D. Krambeck, "An Introduction to Digital Signal Processing - Technical Articles," 2015. https://www.allaboutcircuits.com/technical-articles/an-introduction-to-digital-signal-processing/ (accessed May 29, 2021).

[27] A. Ibrahim, P. Gastaldo, H. Chible, and M. Valle, "Real-time digital signal processing based on FPGAs for electronic skin implementation," *Sensors (Switzerland)*, vol. 17, no. 558, p. 558, 2017.

[28] U. S. Shanthamallu, S. Rao, A. Dixit, V. S. Narayanaswamy, J. Fan, and A. Spanias, "Introducing Machine Learning in Undergraduate DSP Classes," 2019.

[29] M. Kandlhofer, G. Steinbauer, S. Hirschmugl-Gaisch, and P. Huber, "Artificial intelligence and computer science in education: From Kindergarten to university," 2016.

[30] T. Barik, M. Everett, R. E. Cardona-Rivera, D. L. Roberts, and E. F. Gehringer, "A community college blended learning classroom experience through Artificial Intelligence in Games," 2013.

[31] I. Umut and G. Çentik, "Detection of Periodic Leg Movements by Machine Learning Methods Using Polysomnographic Parameters Other Than Leg Electromyography," *Comput. Math. Methods Med.*, vol. 2016, no. 1, pp. 1–7, 2016.

[32] T. Roland, W. Baumgartner, S. Amsuess, and M. F. Russold, "Signal evaluation of capacitive EMG for upper limb prostheses control using an ultra-low-power microcontroller," in *IECBES 2016 - IEEE-EMBS Conference on Biomedical Engineering and Sciences*, 2016, pp. 317–320.

[33] B. Vescio, R. Nisticò, A. Augimeri, A. Quattrone, M. Crasà, and A. Quattrone, "Development and Validation of a New Wearable Mobile Device for the Automated Detection of Resting Tremor in Parkinson's Disease and Essential Tremor," *Diagnostics*, vol. 11, no. 2, p. 200, 2021.

[34] J. Han, "Application of EMG fatigue detection algorithm in portable DSP system," *Acta Tech. CSAV (Ceskoslovensk Akad. Ved)*, vol. 62, no. 3, pp. 85–94, 2017.

[35] J. Zhang, C. Ling, and S. Li, "Human movements classification using multi-channel surface EMG signals and deep learning technique," in *Proceedings - 2019 International Conference on Cyberworlds, CW 2019*, Oct. 2019, pp. 267–273.

[36] Y. Kovalev, T. Bergaliyev, and S. Sakhno, "An Interactive System for the Study of EMG Signal ML-Processing and Prototyping of Human-Machine Interfaces," in *2020 International Conference Engineering and Telecommunication (En&T)*, Nov. 2020, pp. 1–3, Accessed: May 30, 2021. [Online]. Available: https://ieeexplore.ieee.org/document/9431317/.

[37] J. Roy, M. A. Ali, M. R. Ahmed, and K. Sundaraj, "Machine learning techniques for predicting surface EMG activities on upper limb muscle: A systematic review," in *Lecture Notes of the Institute for Computer Sciences, Social-Informatics and Telecommunications Engineering, LNICST*, 2020, pp. 330–339.

[38] Y. Li, K. K. Ang, and C. Guan, "Digital Signal Processing and Machine Learning," in *Brain-Computer Interfaces. The Frontiers Collection.*, Graimann B.;, Pfurtscheller G.;, and Allison B., Eds.

Springer, Berlin, Heidelberg, 2009, pp. 305–330.

[39] G. S. Randhawa, K. A. Hill, and L. Kari, "ML-DSP: Machine Learning with Digital Signal Processing for ultrafast, accurate, and scalable genome classification at all taxonomic levels," *BMC Genomics*, vol. 20, no. 1, 2019.

MUSCULOSKELETAL DISORDER ANALYSIS-ADVANCED IN MEDICAL TECHNOLOGY: SHORT REVIEW

Tengku Nor Shuhada[1,*], Abdul Rahim Abdullah[1] , Norhashimah Mohd Saad[2], Rubita Sudirman[3] and Ezreen Farina Shair[1]

[1]Advanced Digital Signal Processing Laboratory, Faculty of Electrical Engineering, Universiti Teknikal Malaysia Melaka, Malaysia.
[2]Department of Electrical Electronic, Faculty of Engineering and Technologies, Universiti Teknikal Malaysia Melaka (UTeM), Malaysia
[3]School of Electrical Engineering, Universiti Teknologi Malaysia, 81310 UTM Johor Bahru, Johor, Malaysia

[*]Corresponding Author's Email: [1]abdulr@utem.edu.my

Article History: Received June 15, 2021; Revised July 6, 2021; Accepted July 16, 2021

ABSTRACT: Musculoskeletal disorders (MSDs) affect people all over the world and are the second leading cause of disability in the workplace. There are many methods used to analyse MSDs to know the real situation and affected on the employees. The review is to compare in terms of design the findings, methodology, approach and identify the method, sample size, and what they have found from the previous researchers that have many advantages dan disadvantages of the method to come out the best suggestion of proper method to used and suggestion method to explore more for the future researchers. The following technique was used to find relevant literature. After scoping research into different types of MSDs analysis techniques, keywords were found by focusing on the method and approach. The study found that most of the methods in MSD more focus on the Questionnaire as the Method of data in analysis for MSD. However, it is more to after injuries of MSDs happened, but not focusing on a method to avoid the MSD from happed. Thus, involving EMG signal is the proper way to identify MSDs problem with considering the current trend and suggestion from rehabilitation as SOCSO. This paper provides the suggestion method strategies for the researcher of the future to go further in MSD to tackle the more interesting and important information for MSD in the future.

***KEYWORDS**: Musculoskeletal Disorders (MDSs), Method Analysis, Lower Back Pain*

(LBD), Upper Limb Disorders (ULDs), Lower Limb Disorders (LLDs)

1.0 INTRODUCTION

MSD is a worldwide occupational health issue that is now being debated. In Malaysia, there has been an upward tendency in recent years, especially in the manufacturing sector [1]. One of the most common causes of workplace accidents and disabilities in the healthcare field is musculoskeletal disorders (MSDs) and injuries. Construction is regarded as the most dangerous activity when opposed to other sectors [2].

As a result, in many high-income nations, it has become a well-known topic in safety research [3]. Manual handling, heavy lifting, repetitive work, and difficult jobs have all been identified and documented workplace risk, issues caused by rapid exertion or excessive exposure to physical factors [3][4]. Muscles, nerves, tendons, joints, cartilage, and supporting tissues of the upper and lower limbs, spine, and lower back will be affected by these issues [5].

Musculoskeletal disorders (MSDs) affect people all over the world and are the second leading cause of disability in the workplace. These disorders account for 40-50 percent of the total cost of all work-related illnesses [6][7]. Furthermore, 50% of all more than 3 days' absences from work and 49% of all more than two-week absences cause by MSDs. The quantity, speed, and amount of power exerted with each movement are all directly related to the risk disorder [6], [8]. Muscle performance is the key to know the muscle recovery and suggest the average effect for intensive nixed exercise for strength and endurance exercise and massage to more effective for the subjects [9].

Some medical technologies, such as equipment and analysis methods, have been used to understand or measure the situation of MSD among humans, whether they are employees or have a history of accidents [10],[11]. It is being referred to as any tissue damage to the musculoskeletal and nervous systems, which affect organ function [12]. This study aims to know in detail about the previous method used to analyse MSDs issues and what the method offered to know the performances of MSD for particular mentioned. Thus, from the

study of previous techniques of MSDs analysis, it will able to know more detail about the advantage and disadvantages of all the methods used by researchers before.

1.1 Types of MSDs

Low Back Pain (LBP)

Low back pain is a very common symptom and becomes the most common MSD is back pain [13]. It affects people of all ages, from children to the elderly, in high-income, middle-income, and low-income countries. Between 1990 and 2015, the number of years spent disabled by low back pain rose by 54% globally, potentially arise from population growth and aging, with the greatest increases occurring in low- and middle-income countries, such as Asia, Africa, and the Middle East. Low back pain is now the most common cause of disability in the globe [14], and in areas where adequate resources to address the problem are lacking, the consequences are likely to be more severe [15]. Figure 1 shows the position of lower back pain in the human body.

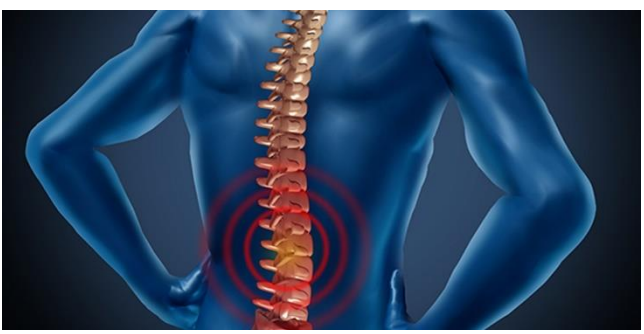

Figure 1: Lower Back Pain (LBP)

Upper Limb Disorders (ULDs)

Any injury or disease affecting the upper limbs, from the fingertips to the shoulder or spine, is classified as an upper limb disorder. Work-related musculoskeletal conditions are the most common occupational health problem in the UK, accounting for about 40% of sickness absences in the NHS. Work-related upper limb diseases (ULDs), which affect the hand, wrist, arm, shoulder, and neck, affect 700 people per 100,000 in the UK [16]. Because of the nature of anaesthetists' work, they are at an increased risk of bad posture,

which can contribute to the development of upper limb diseases. Figure 2 shows the position of upper limb disorders in the human body.

Figure 2: Upper Limb Disorder (ULDs)

Lower Limb Disorders (ULDs)

Injury and abnormalities of the lower limbs, ranging from the hip to the toes. Work-related musculoskeletal illnesses are a significant financial burden on society and one of the leading causes of lost productivity due to illness [17]. Work-related health problems have significant expenses for their employers, in addition to the apparent effects for the individual. Many researchers have looked into the prevalence of and risk factors for work-related upper limb, neck, and low back diseases [18]. However, when compared to other work-related musculoskeletal complaints in the upper body or low back pain, lower limb issues have received less attention. Lower limb disorder in the human body are shown in Figure 3 [19].

Figure 3: Lower Limb Disorders (LLD)

2.0 RESULTS AND DISCUSSION

2.1 Musculoskeletal Disorders (MSDs) analysis

Table 1: Types of method analysis of Musculoskeletal Disorders (MSD)

Authors	Objectives	Method	Sample Size	Results
[20]	MSD with depression as a mediator among school teachers to examine psychosocial aspects	Answer the Work Organization Assessment Questionnaire (WOAQ) Statistical Package for Social Science (SPSS)	367 respondents	80.1 % (95 percent confidence interval: 75.8–84.2 %), with 80.5 % of female teachers and 77.5 % of male instructors experiencing symptoms at that time
[11]	Improve the features of Health Screening Test System (HSTS) for MSD	development of HSTS evaluation Functional Range of Motion (FROM)	20	constructed for evaluating the plan, comparing it to the MTM standard, and providing criticism
[21]	Men and women veterans with TMD were compared in terms of MS, pain, and mental health comorbidities.	For cross-sectional analysis, chi-square tests, t tests, and logistic regression were used.	NA	Odds of TMD were higher in men of Hispanic ethnicity (OR¼1.38, 95% CI ¼ 1.27–1.48) and

[22]	During treadmill walking, electromyography (EMG) signals were obtained.	The significant level of EMG activity was determined using a paired sample t test.	105	The t-test was used to determine the significance level of EMG activity, and the results revealed significant differences between the right and left side packs.
[23]	identify the related factors of a taking healthy sitting posture in office workers	qualitative study aimed to use the theoretical domains framework (TDF)	25	Skills, knowledge, and behavioural regulation are among the TDF domains that have been mapped.
[24]	EMG signal categorization for a health screening job for musculoskeletal disorders	Functional Range of Motion (FROM)-time-frequency method- spectrogram -classification- k-Nearest Neighbor (k-NN), Linear Discriminant Analysis (LDA), Nave Bayes (NB), and Support Vector Machine are machine learning classifiers	5	LDA is the best classifier method for classify emg signal with features Mean Vrms (93.33%), standard deviation (80%)
[25]	Utilise the time-frequency spectrum obtained using generalised Warblet transform (GWT) for EMG fatigue analysis.	Time-frequency spectrum	20	In non-fatigue conditions, the IMNF, IMDF, and ISPEn increased by percentage, 34 %, and 36 %, respectively. In contrast, weariness is associated with a 22 % ISSkw.
[26]	cross-sectional - to determine musculoskeletal work related pain	Standardized Nordic Questionnaire (SNQ) Data so obtained was analysed using Statistical Package for Social Science (SPSS) Version-16 data analysis software	60	prevalence of musculoskeletal problems in the present study was found to be 68.3%
[27]	investigate the prevalence of musculoskeletal disorders (MSDs) in the general population.	Rapid Entire Body Assessment method	51	neck (47%), shoulder (51%), lower back (43%), and knee (47%)

[28]	suggest signal processing approaches for evaluating the temporal and spectral changes in characteristics of the surface myoelectric signal in different patient groups to investigate the electrical manifestations of neuromuscular disease using time-frequency	Continues Wavelet Transform (CWT) Mean absolute value, the energy, standard deviation as temporal parameters, total and mean power as frequency parameters	3- Normal, Myopathic and Neuropathic subjects	Neuropathy is the most severe pathology, accounting for 10% to 85% of cases, with an average of 47.5 %

Table 1 shows the topic method used to analyse musculoskeletal disorders. There are some of the methods used for method analysis MSD in the previous researchers, which are questionnaire, statistic analysis, qualitative analysis, and some of the articles is involving electromyography for time-frequency analysis and combining with classification method, and development of the technology to make it easier in interpretations.

From all results in the table, total and mean power are frequency parameters, while mean absolute value, energy, and standard deviation are temporal parameters [29] and Work Organization Assessment Questionnaire (WOAQ). The purpose of the questionnaire is to investigate how physical function is assessed in people with musculoskeletal disorders (MSD) [30]. This technique is common used by researchers because it can involve more respondents and easy to handle and analyse.

However, The Malaysian Social Security Organisation (SOCSO) has organised a Health Screening Programme (HSP) employing Functional Range of Motion (FROM), which has previously been performed in a rehabilitation clinic, to teach and diagnose patients using normal physical assessment procedures [31]. SOCSO existing functional testing is required the occupational therapist to do the subjective judgment in times of respondent to determine the capability of the patients [24]. The validation of results depends on the time consumed to fulfill the HSP tasks and compared to the standard time to determine the respondent's ability to perform functional reaching tasks (work capacity) [32], [33]. It is shown that to study MSD, the considering of EMG signal is become as one of important to be catered in MSD diagnosis.

Most of the methods in the results table do not accurately reflect the

muscle's condition. The reliability of the effort level determines whether the respondent is fit enough to continue working or not. In SOCSO, the decision is solely reliant on the instructor's decision, which has a significant disadvantage in that the instructor's opinion may be influenced by factors other than visual perception information [34]. Therefore, to solve all the issues, muscle performance is the key to know the muscle recovery and suggest the average effect for intensive nixed exercise for strength and endurance exercise and massage to more effective for the subjects [9].

Recent advancements in rehabilitation have revealed EMG pattern recognition as a promising approach with promise promising technique that has been crucial to use in clinical diagnosis [8]. Electromyography (EMG) signals are bioelectrical signals that are widely used as important tools in rehabilitation for providing information on neuromuscular activity from which it originates that will help to understand the human movements of activities [3], [35], [36]. There has been a lot of research done on MSDs that includes electromyography (EMG) in the activities [19], [37]. EMG is contained rich muscle information that would be used in clinical and rehabilitation applications [38]. The EMG is also used as a device for recording from the muscles' residual limb, and electrical signals have been studied in research to provide information on muscular movements during any human or animal activity [36], [37], [39]. Figure 4 shows the example of EMG signal for muscle inactive (contraction) and rest in baseline.

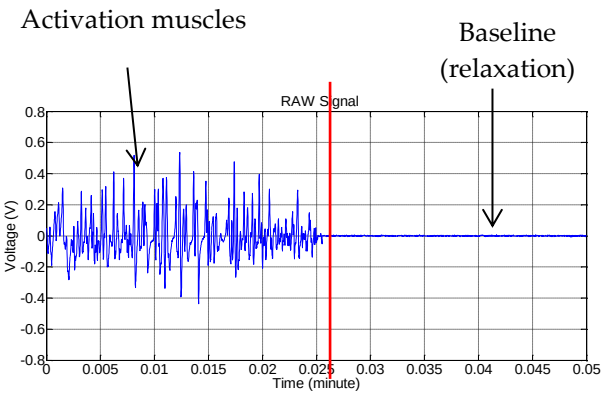

Figure 4: the example of EMG signal

The categorisation of surface electromyography (sEMG) signals is critical in man-machine interfaces for proper control of multiple-degree-of-freedom prosthetic devices. The most important components of this field's research are data gathering, pre-processing, feature extraction, and classification, as well as their practicality in terms of application and reliability [40]. Figure 5 shows the example of classification true and false. Based on this table, it is shown the classification of axial rotational reach is the best compared to kneeling reach and kneeling to standing reach health screening program (HSP) in SOCSO.

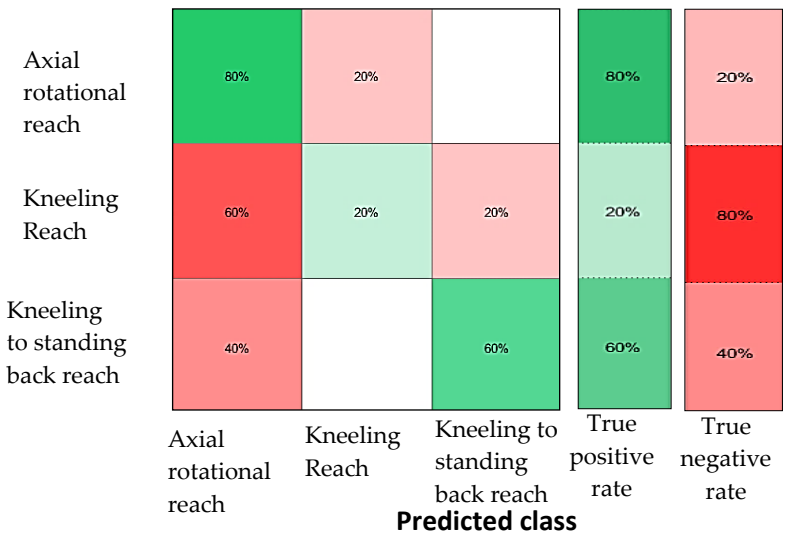

Figure 5: Positive predictive (PPV) and false discovery rate (FDR) for each type of tasks

The EMG classification task has been extensively researched, leading to the creation of a number of methods, including statistically generated mathematical models, discriminative learning models, and genetic algorithm-based strategies [40]. Linear Discriminant Analysis (LDA), Support Vector Machines (SVMs), and Hidden Markov Models (HMM) are three major methodologies for classifying sEMG signals for controlling upper limb prostheses, all of which show a slight improvement in classification accuracy [41]. The including of EMG in MSD is very interesting to explore more in the future analysis of MSD to gain more information, not visualisation but also from inside the body.

3.0 CONCLUSION

Based on the review, it can be confirmed some of the findings from the previous reviews have evaluated relationships between the objectives, method for MSDs analysis, the sample size for the questionnaire (quantitative) and experimental (qualitative) and results from the performance of each method analysis. There is a lack of evidence to perform detailed method analysis to get the results. Further investigations are required to examine more detail about the type of equipment and experiment use to know the performance of MSDs by considering Electromyography (EMG) with the assessment of the muscles inside of the body. The information of equipment and method in the literature can provide the extra understanding the overview of the concept of MSDs analysis and what the important thing is MSD to be considered. Thus, this review paper will be helpful for future investigation and become one of the references to find the method of analysis MSDs by considering on EMG signal. Besides that, this paper provides an overview of a current trend in analyzing of MSDs problem. It can provide more detailed information of the MSDs problem that would be helpful in the classification of the MSD from the muscles performances.

ACKNOWLEDGMENTS

A grateful thanks to the Ministry of Higher Education Malaysia (MOHE), Fakulti Kejuruteraan Elektrik (FKE), Fakulti Teknologi Kejuruteraan Elektrik & Elektronik (FTKEE), Advanced Digital Signal Processing (ADSP) Research Laboratory, Rehabilitation Engineering & Assistive Technology (REAT) Research Group, Center of Robotics & Industrial Automation (CeRIA), Universiti Teknikal Malaysia Melaka (UTeM) for the use of the facilities to complete this project, for sponsoring this work under project F00428 - FRGS/1/2020/FTKEE-CERIA.

4.0 REFERENCES

[1] V. V. and M. Y. M. D. Mohd Zubairy Shamsudin *et al.*, "Work-related

Musculoskeletal Disorders (WMSDs) among Industrial Packaging Workers in Malaysia," *Malaysian J. Hum. Factors Ergon.*, vol. 2, no. 1, pp. 17–24, 2017.

[2] A. M. Shrestha, S., Pradhananga, N. and Sadri, "Understanding the Role of Social Influence on Construction Safety Using an Ego-Centric Network Approach," in *Safety, Workforce, and Education*, 2020, pp. 481–489.

[3] E. F. Shair, S. A. Ahmad, M. H. Marhaban, S. B. M. Tamrin, and A. R. Abdullah, "EMG Processing Based Measures of Fatigue Assessment during Manual Lifting," *Hindawi*, vol. 2017, pp. 1–12, 2017.

[4] M. N. A. R. Nur A' Tifah Jaffar, "Review on risk factors related to lower back disorders at workplace Review on risk factors related to lower back disorders at workplace," in *IOP Conference Series: Materials Science and Engineering PAPER*, 2017, pp. 1–9.

[5] T. Rice *et al.*, "Revisiting out-of-pocket requirements: Trends in spending, financial access barriers, and policy in ten high-income countries," *BMC Health Serv. Res.*, vol. 18, no. 1, pp. 1–18, 2018.

[6] H. Daneshmandi, A. R. Choobineh, H. Ghaem, M. Alhamd, and A. Fakherpour, "The effect of musculoskeletal problems on fatigue and productivity of office personnel: A cross-sectional study," *J. Prev. Med. Hyg.*, vol. 58, no. 3, pp. E252–E258, 2017.

[7] V. V. and M. Y. M. D. Mohd Zubairy Shamsudin, "Work-related Musculoskeletal Diorders (WMSDs) Among Industrial Packaging Workers in Malaysia," *Malaysian J. Hum. Factors Ergon.*, vol. 2, no. 1, pp. 17 – 24, 2017.

[8] A. R. A. Hamid *et al.*, "Causes of fatal construction accidents in Malaysia," in *IOP Conference Series: Earth and Environmental Science*, 2019, vol. 220, no. 1, pp. 1–14.

[9] W. Poppendieck, M. Wegmann, and A. Ferrauti, "Massage and Performance Recovery : A Meta-Analytical Review," *Sport. Med.*, vol. 46, no. 2, pp. 183–204, 2016.

[10] M. M. Cremasco, A. Giustetto, F. Caffaro, A. Colantoni, E. Cavallo, and S. Grigolato, "Risk assessment for musculoskeletal disorders in forestry: A comparison between RULA and REBA in the manual feeding of a wood-chipper," *Int. J. Environ. Res. Public Health*, vol. 16, no. 5, 2019.

[11] A. R. Abdullah *et al.*, "An Improved Features of Health Screening Test System for Malaysian Social Security Organisation (SOCSO) Programme," *Indones. J. Electr. Eng. Comput. Sci.*, vol. 6, no. 2, pp. 473–481, 2017, doi: 10.11591/ijeecs.v6.i2.pp473-481.

[12] A. Nowadays, "Status of Musculoskeletal Pains and Disorders among Computer Users," vol. 3, no. 3, pp. 83–86, 2018.

[13] A. G. Patiño, M. Khoshnam, and C. Menon, "Wearable device to monitor back movements using an inductive textile sensor," *Sensors (Switzerland)*, vol. 20, no. 905, pp. 1–17, 2020.

[14] J. Hartvigsen *et al.*, "What low back pain is and why we need to pay attention," *Lancet*, vol. 391, no. 10137, pp. 2356–2367, 2018.

[15] R. Buchbinder *et al.*, "Low back pain: a call for action," *Lancet*, vol. 391, no. 10137, pp. 2384–2388, 2018.

[16] S. Leifer, S. W. Choi, K. Asanati, and S. M. Yentis, "Upper limb disorders in anaesthetists – a survey of Association of Anaesthetists members," *Anaesthesia*, vol. 74, no. 3, pp. 285–291, 2019.

[17] D. Starovoytova, "Hazards and Risks at Rotary Screen Printing (Part 2 / 6): Analysis of Machine-operators' Posture via Rapid-Upper-Limb-Assessment (RULA)," *Ind. Eng. Lett.*, vol. 7, no. 5, pp. 42–63, 2017.

[18] M. G. Garcia, M. Graf, and T. Läubli, "Lower limb pain among workers: a cross-sectional analysis of the fifth European Working Conditions Survey," *Int. Arch. Occup. Environ. Health*, vol. 90, no. 7, pp. 575–585, 2017.

[19] S. Sen and A. D. Singh, "Electromyographic Analysis of Upper Trapezius Muscle and Development of MSD in Collegiate Students Carrying Laptop Bag," *Am. J. Sport. Sci.*, vol. 4, no. 6, pp. 120–124, 2016.

[20] Y. M. Ng, P. Voo, and I. Maakip, "Psychosocial factors, depression, and musculoskeletal disorders among teachers," *BMC Public Health*, vol. 19, no. 1, pp. 1–10, 2019.

[21] B. T. Fenton, J. L. Goulet, M. J. Bair, T. Cowley, and R. D. Kerns, "Relationships between temporomandibular disorders, msd conditions, and mental health comorbidities: Findings from the veterans musculoskeletal disorders cohort," *Pain Med. (United States)*, vol. 19, pp. S61–S68, 2018.

[22] C. Students, C. Laptop, S. Sen, and A. D. Singh, "Electromyographic Analysis of Upper Trapezius Muscle and Development of Electromyographic Analysis of Upper Trapezius Muscle and Development of MSD in Collegiate Students Carrying Laptop Bag," no. August, 2018, doi: 10.11648/j.ajss.20160406.14.

[23] P. Hosseini-Koukamari, M. Ghaffari, S. Tavafiyan, and A. Ramezankhani, "Using Theoretical Domains Framework for Exploring Appropriate Sitting Posture Determinants Among Office Workers: A Content Analysis Study," *Heal. Scope*, vol. 10, no. 1, 2021.

[24] T. Nor, S. Tengku, A. R. Abdullah, E. F. Shair, and N. M. Saad, "Classification of EMG Signal for Health Screening Task for Musculoskeletal Classification of EMG Signal for Health Screening Task for Musculoskeletal Disorder," *Int. J. Eng. Technol.*, vol. 8, no. 1.7, pp. 219–226, 2019.

[25] D. M. Ghosh and R. Swaminathan, "Generalised Warblet transform-based analysis of biceps brachii muscles contraction using surface electromyography signals," *Int. J. Biomed. Eng. Technol.*, vol. 34, no. 4, pp. 305–318, 2020.

[26] H. S. Bedi, N. J. Moon, V. Bhatia, G. K. Sidhu, and N. Khan, "Evaluation of musculoskeletal disorders in dentists and application of DMAIC technique to

improve the ergonomics at dental clinics and meta-analysis of literature," *J. Clin. Diagnostic Res.*, vol. 9, no. 6, pp. ZC01–ZC03, 2015.

[27] M. R. Khan and N. K. Singh, "Prevalence of musculoskeletal disorders among Indian railway sahayaks," *Int. J. Occup. Environ. Health*, vol. 24, no. 1–2, pp. 27–37, 2018.

[28] A. Mokdad, S. M. El Amine Debbal, and F. Meziani, "Application of the continuous wavelet transform for the analysis of pathological severity degree of electromyograms (EMGs) signals," *Polish J. Med. Phys. Eng.*, vol. 26, no. 3, pp. 149–154, 2020, doi: 10.2478/pjmpe-2020-0017.

[29] M. C. Gutierrez-Diez, M. A. Benito-Gonzalez, R. Sancibrian, M. A. Gandarillas-Gonzalez, C. Redondo-Figuero, and J. C. Manuel-Palazuelos, "A study of the prevalence of musculoskeletal disorders in surgeons performing minimally invasive surgery," *Int. J. Occup. Saf. Ergon.*, vol. 24, no. 1, pp. 111–117, 2018.

[30] B. Wiitavaara and M. Heiden, "Content and psychometric evaluations of questionnaires for assessing physical function in people with neck disorders: a systematic review of the literature," *Disabil. Rehabil.*, vol. 40, no. 19, pp. 2227–2235, 2018, doi: 10.1080/09638288.2017.1334096.

[31] R. C. M. David J. Magee, *Orthopedic Physical Assessment - E-Book*. 2021.

[32] E. Abdek-Moty *et al.*, "Functional Capacity and Residual Functional Capacity and Their Utility in Measuring Work Capacity. The Clinical Journal of Pain, 9(3), 168–1.pdf," *Clin. J. Pain*, vol. 9, no. 3, pp. 168–172, 1993.

[33] E. F. Shair, "Core Lifting Task Assessment Using Time-Frequency," 2019.

[34] J. T. Herbert, Y. Zhai, and W. Coduti, "Employment Among Rehabilitation Counselors," *J. Rehabil.*, vol. 86, no. 1, pp. 32–40, 2020.

[35] U. Sahin, "Pattern Recognition with surface EMG Signal based Wavelet Transformation," pp. 295–300, 2012.

[36] O. W. Samuel *et al.*, "Pattern recognition of electromyography signals based on novel time domain features for amputees' limb motion classification," *Comput. Electr. Eng.*, vol. 67, pp. 646–655, 2018.

[37] T. Ghosh, "Assessment of Postural effect on Work Related Musculoskeletal Disorders and Back Muscle Fatigue among the Goldsmiths of India Abstract :," *Int. J. Occup. Saf. Heal.*, vol. 5, no. 2, pp. 16–22, 2015.

[38] J. Too, A. R. Abdullah, N. M. Saad, N. M. Ali, and H. Musa, "A Detail Study of Wavelet Families for EMG Pattern Recognition," *Int. J. Electr. Comput. Eng.*, vol. 8, no. 6, p. 4221, 2018, doi: 10.11591/ijece.v8i6.pp4221-4229.

[39] J. Kilby, K. Prasad, and G. Mawston, "Multi-channel surface electromyography electrodes: A review," *IEEE Sens. J.*, vol. 16, no. 14, pp. 5510–5519, 2016.

[40] A. K. Mukhopadhyay and S. Samui, "An experimental study on upper limb position invariant EMG signal classification based on deep neural network,"

Biomed. Signal Process. Control, vol. 55, p. 101669, 2020.

DEVELOPMENT ON SLEEP MONITORING SYSTEM CONFIGURATION TOWARD AN OPTIMAL AMBIENT CONDITION SETTING OF THE SLEEP QUALITY

W.H.M. Saad[1,*], A.S.M. Shokri[2], S.A. Radzi[1], S.J.A. Razak[3] and M.N.S. Zainudin[1]

[1]Faculty of Electronics and Computer Engineering.
[2]Faculty of Electrical and Electronics Engineering Technology.
Universiti Teknikal Malaysia Melaka, Durian Tunggal, 76100, Melaka, Malaysia.

[3]SolokFertigasi by MSJ Perwira Enterprise.
75460 Duyong, Melaka, Malaysia.

[*]Corresponding Author's Email: [1]wira_yugi@utem.edu.my

Article History: Received July 1, 2021; Revised July 12, 2021;
Accepted July 16, 2021

ABSTRACT: Sleep is a form of rest and getting enough sleep at the right times with suitable surrounding conditions is very important to maintain good health throughout life. The study aims to develop the end-user prototyping for a sleep monitoring system that measures the room ambient and body condition by using a wireless device utilizing Bluetooth Low Energy (BLE) embedded system. For the user interface, the Window application is used to display the collected data from separate ambient parameters and body condition embedded systems using Bluno Uno and Bluno Nano respectively. This sleep monitoring system is also equipped with a video and audio recording from the web camera and microphone of the built-in PC-based unit. Capturing data from body monitoring and ambient monitoring separate units are then transferred to the Window based application by using the BLE connection and lastly, the captured data are log into the MySQL database with the date and time stamp. The ambient condition system captured the room temperature and humidity, light intensity and rate of CO_2 concentration. The body condition system, it is measuring body temperature, heart rate and body movement. Based on the device testing on sleep monitoring, each of the parameters measured is optimized to choose the best possible occurrence of ambience setting selection for optimal sleep quality.

***KEYWORDS**: Sleep Monitoring Systems; Ambient Monitoring Systems; Body*

Monitoring Systems; Bluetooth Low Energy (BLE).

1.0 INTRODUCTION

Sleep satisfaction is one of the keys to achieving the ultimate goal of a healthy body. While in sleep, our body is resting and conserving energy while restoration our tissues and cognitive function, emotion regulation, and immune health [1]. The pathological changes to our hormonal balance in the body between glycogen and adenosine after waking up from enough sleep making us feel refresh. Most of the restoration of energy occur while in non-REM sleep or also known as deep sleep [2]. On the other hand, the rapid eye movement (REM) sleep stage is when our eye is moving in a range of directions without sending any visual information to the brain [2]–[4]. Dreams often occur while in REM sleep and that is why REM sleep is also known as dream sleep. While sleeping with eyes closed, REM can be measured by using Electromyograph (EMG) device with electrodes located surrounding the eyes. Some other physiological body condition also varies while we are sleeping and this includes brain activity, body temperature, heart rate, oxygen level, carbon dioxide level and breathing rate [2]. This parameter often uses by the monitoring system that falls either under medical devices or consumer products to represent sleep quality.

The sleep monitoring system function as a device to quantify the parameter of sleep quality representation characteristic based on its purpose [5]–[8]. For example, a medical-grade device that is used to measure obstructive sleep apnea (OSA) often utilises the pneumotachograph sensor, nasal pressure transducer, and oronasal thermal sensor with pulse oximetry to diagnose the abnormality in airflow, snoring breathing rate and oxygen level to diagnose the patient. On the other hand, the sleep monitoring device for personal daily use often measure heart rate and movement and estimated the quality of the sleep based on the continuous pattern and behaviour of the measured data.

In this study, the aim is to propose the development of a sleep monitoring device for personal use that incorporated ambient and body condition measurement to get more insight on making a deductive interpretation toward an optimum sleep quality. Previously, such a conceptual system has been proposed in [7], [9] and with an additional measurement parameter that is done in this study, it requires a simple modification on device development configuration

and validation measurement that is emphasized by this manuscript. The functionality presented by the proposed device allowing the user to escalate the best surrounding condition that highly contribute to their personalise sleep preferences requirement to achieve a good sleep quality by customizing the ambient itself.

This paper consists of four major sections including this section. Section 2.0 consists of the methodology development of the sleep monitoring system for the body and ambient. Then, Section 3.0 encompasses the experiment result from on-device testing and discussion. Lastly, Section **Error! Reference source not found.** concludes the work and future direction.

2.0 METHODOLOGY

The proposed sleep monitoring system consists of two parts which are the ambient condition system and body condition system. An ambient condition system as shown in Figure 1 equipt with a sensor that can measure the surrounding environment such as temperature, humidity, light intensity, noise and quality of air.

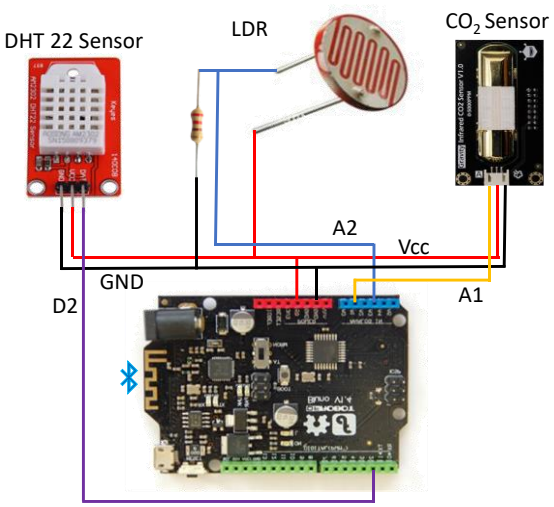

Figure 1: Circuit configuration for ambient monitoring system

For the body condition system as shown in Figure 2, the sensor will monitor the body condition of the user while sleeping such as heart rate, body temperature and body movement. Both systems are equipped with Bluetooth Low Energy (BLE) connectivity and readings generated from both systems were collected by using PC for data

logging and visualisation. Both systems consist of a microcontroller that is programmed by using Arduino IDE and the Window Application that will display the readings was designed by using Microsoft Visual Studio 2015. The architecture of the sleep monitoring system can be seen in Figure 3.

For the ambient monitoring system, BLUNO UNO is working with a digital temperature and humidity sensor (DHT22), a light-dependent resistor (LDR) and a CO_2 gas sensor to capture the reading of light intensity, humidity, room temperature and quality of air in the surrounding ambient where the user sleep. Then, in the body condition system, BLUNO NANO is working with a pulse sensor, accelerometer and thermistor to capture the reading of heart rate, body temperature and body movement while the user is sleeping. The functional prototype of the ambient condition system and body condition system has been designed and prepared as shown in Figure 4. From the figure, the prototype of the body condition system has been designed in the form of a wearable belt that will be wear as a chest strap by the user during sleep and on the other hand, the prototype of the ambient condition system will be placed on the bedside table next to where the user is sleeping as shown in Figure 5.

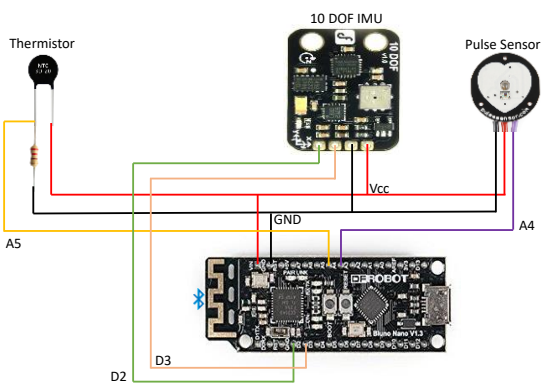

Figure 2: Circuit configuration for body condition monitoring system

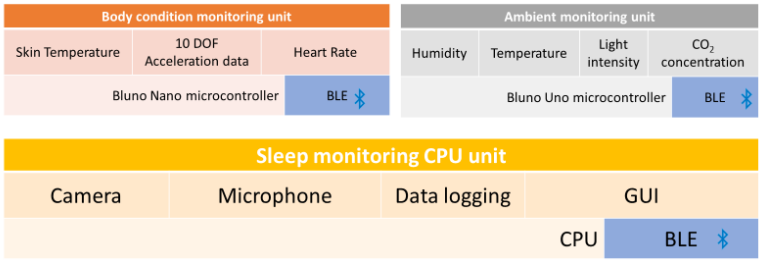

Figure 3: Sleep monitoring system software architecture

The data captured by both systems were transferred to window apps via Bluetooth connection. Window apps were designed using Microsoft Visual Studio 2015 will display the readings that have been received and logged the data into the MySQL database. Several tables were created in the database to update the time and value of each parameter. In addition, users can enable the video and audio recording functionality from a camera and microphone of the PC. Figure 6 shows the GUI of the sensor status triggered from both ambient and body condition monitoring systems on the designed Window Apps.

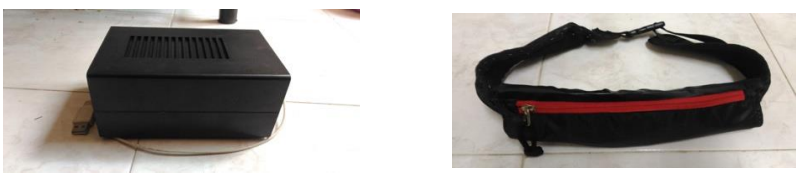

(a) (b)

Figure 4: Prototype of (a) ambient and (b) body condition monitoring system

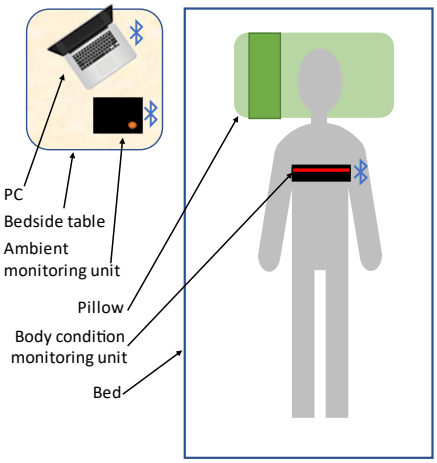

Figure 5: Scenario of the sleep monitoring system while the subject is on the bed

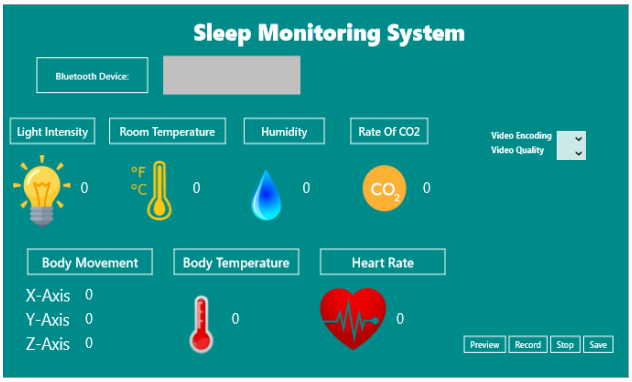

Figure 6: Graphical user interface (GUI) of Sleep monitoring system application

In general, the flowchart of the overall development methodology can be seen in **Error! Reference source not found.**. The development starts with circuit design and fabrication for each monitoring system then followed by GUI development on Window Apps then continued by communicating each microcontroller used with the application on Window apps through serial communication port through BLE.

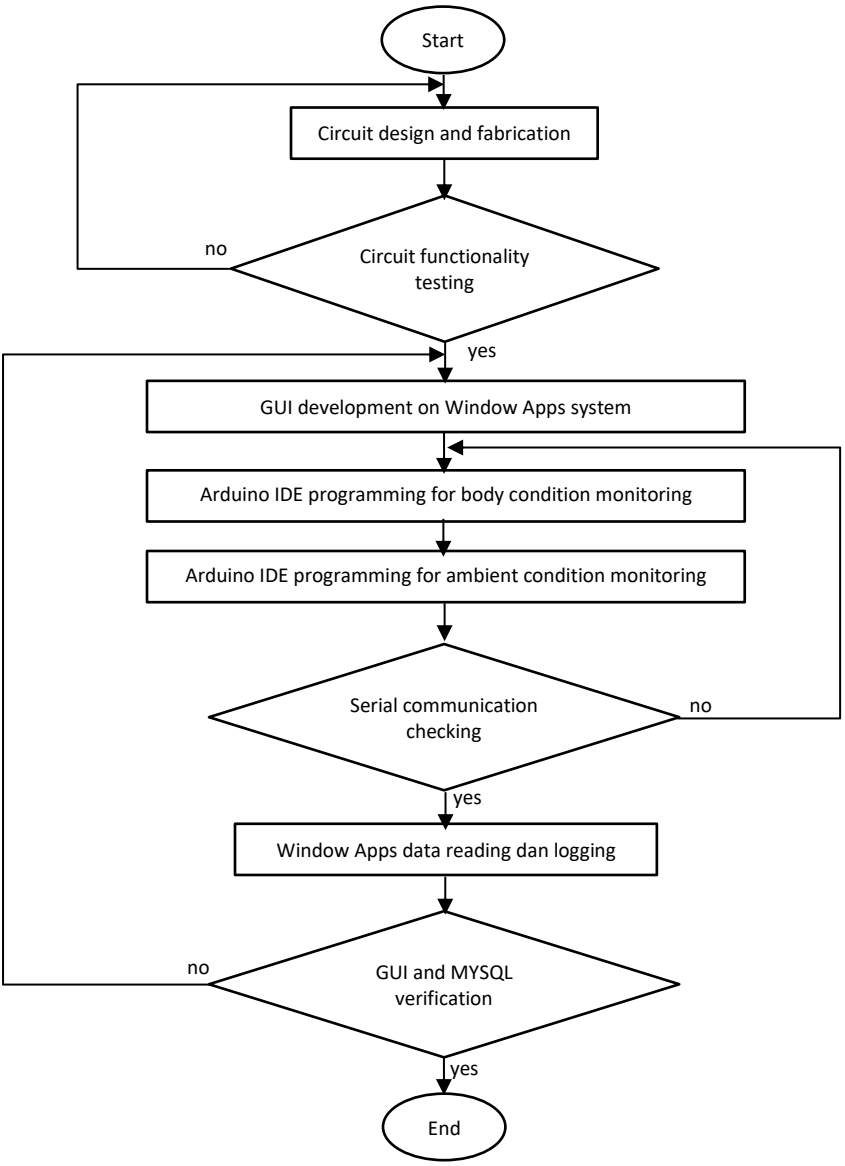

Figure 7: Overall methodology of sleep monitoring system development

To use the sleep monitoring system, both the ambient condition system and body condition system need to be power on first. The body condition system was designed to be powered up by using a rechargeable lithium-polymer battery for portability as it is directly fitted on the user body while

the ambient condition system can be directly power up through a USB connection plug giving a convenient option to the user either to plug it directly on the PC or plug it into the USB power source. A lithium polymer battery also called LiPo battery is chosen to supply sufficient power to the body condition system as it is rechargeable, light and smaller and it can power up the system all night long without running out of battery.

The second step is to pair both systems that have been powered on with PC through Bluetooth>Manage Bluetooth Device on system setting using with preset pairing password. Once it is paired, it will appear as "Bluno.Core.BlunoDevice" in the Bluetooth device list view in the Apps. GUI indicating both devices have been connected to the PC. Then, the Windows application will display the reading captured from the microcontroller. Windows application will ask the user permission to access the camera and audio. When it already gets permission, the video and audio recorder can be used by clicking on the "Record" button to logging all the parameters.

3.0 RESULT AND DISCUSSION

When getting ready, all the equipment is turned on and paired to the PC accordingly. Before going to sleep, the subject had to wear the belt stripe of the body condition monitoring system at the chest and hit the record button on the GUI of Window Apps.

The experiment was carried out on a few different surrounding conditions to observe the effect of the individual perception on ambient conditions toward sleep quality. The experiment is done based on the normal sleep hour of the subject and the quality of sleep is measured based on the estimated duration of sleep transition. The example of the recorded data for both monitoring systems in the MySQL database is extracted and plot as can be seen in Figure 8 and Figure 9. From the plot of Figure 8, the sleep cycle from transition to light sleep, dream sleep and deep sleep is estimated based on the work done in [7], [9] where body conditions such as body temperature, heart rate and body movement are determined the sleep cycle stages.

Four parameters of ambient were investigated which are temperature, light intensity, humidity and CO_2 concentration on the air as each of these parameters were reported to give some of the effects toward sleep quality [10]–[15]. Even though the parameter of the ambient is measured accurately by the sensor but in this study, the perception of the subject is what mostly matters in this experimental

observation and at the same time, it is easier to control and maintain the value [16], [17]. The details on the ambient parameter perception set-up are listed in Table 1. Since CO_2 concentration in the air can be affected by improper air ventilation in the bedroom throughout sleep time [11], the experiment is focused on the comparison between good air ventilation and improper air ventilation.

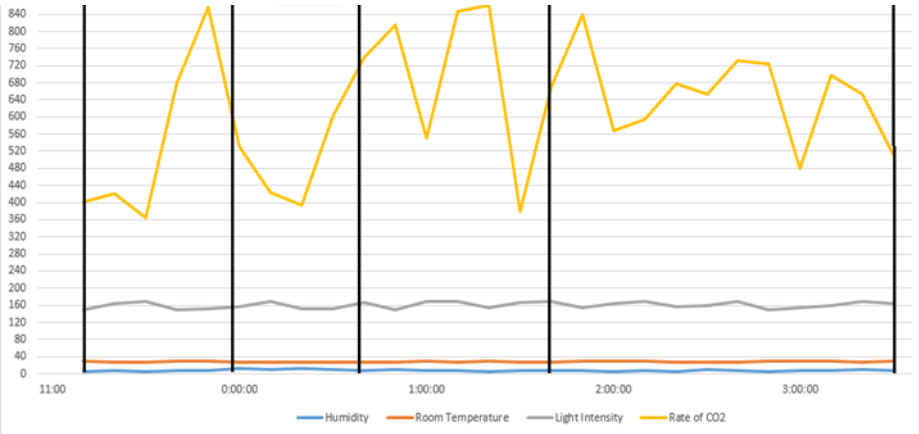

Figure 8: Changes in ambient condition measured

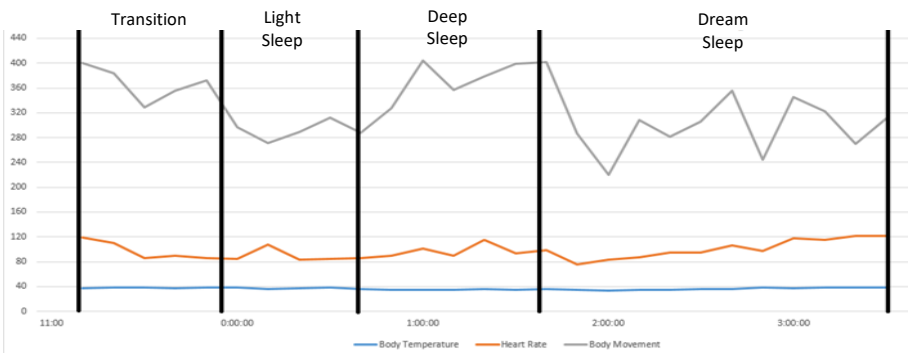

Figure 9: Changes in body condition measured

After that, the ambient condition system is placed on the table beside the bed where the sample is sleeping. The experiment is ready to start as all the connections have been done. In addition, the experiments are carried out starting when the sample sleep until the sample wakes up to observe any changes in the body condition to analyze the quality of sleep of the subject in their usual sleeping bedroom.

The main objective of running this experiment is to investigate preliminary in terms of each of the ambient parameters that can give effect to the duration of deep sleep and REM sleep. The measurement

of each set was repeated for three-night nonconsecutively and the average measuring time was recorded and can be seen in Table 2. Each of the parameters is set up by turning on the devices uses with similar parameters each time it has been used to resulting in a similar control environment every time the experiment took place. The city location where the experiment took place is in Melaka, Malaysia (2.1896° N, 102.2501° E) where the climate here is hot and humid throughout the year.

Table 1: Four settings of ambient parameter set up

Ambient parameters	Perception	A targeted condition set up	Other control parameters
Setting 1: Humidity	(a) Humid	The humidifier was turn on	• The airconditioning was turn on • The light was turn off • The ventilation fan was turned on
	(b) Normal	The humidifier was turn off	
Setting 2: Room Temperature	(a) Cool	The airconditioning was turn on	• The light was turn off • The ventilation fan was turned on • The humidifier was turn on
	(b) Normal	The airconditioning was turn off	
Setting 3: Light intensity	(a) Bright	The light was turn on	• The airconditioning was turn on • The ventilation fan was turned on • The humidifier was turn on
	(b) Dark	The light was turn off	
Setting 4: CO_2 concentration/ Air Ventilation	(a) Good ventilation	The ventilation fan was turned on	• The airconditioning was turn on • The light was turn off • The humidifier was turn on
	(b) Poor ventilation	The ventilation fan was turned off	

Table 2: Average time taken of each sleep cycle for different parameters conditions of the ambient setting.

Ambient Parameter Setting	Average Taken Time in Hours and Minutes (HH:MM)					
	Transition	Light Sleep	Deep Sleep	REM Sleep	Total Sleep	Deep Sleep+REM Sleep
Setting 1(a)	00:31	00:57	01:09	02:48	05:27±00:12	03:58
Setting 1(b)	00:23	00:27	01:29	02:48	05:08±00:06	04:18
Setting 2(a)	00:26	00:48	01:08	03:08	05:31±00:18	04:16
Setting 2(b)	00:25	01:22	00:33	03:20	05:41±00:15	03:53
Setting 3(a)	00:24	01:25	00:31	03:22	05:43±00:10	03:54
Setting 3(b)	00:24	00:47	01:07	03:13	05:33±00:23	04:21
Setting 4(a)	00:22	01:15	00:40	03:16	05:35±00:16	03:56
Setting 4(b)	00:22	00:55	01:07	03:03	05:29±00:09	04:11

Based on the result shown in Table 2, generally, in most of the cases, the subject took about three hours in the dream sleep mode and 30 minutes to 1 hour in deep sleep mode. Comparatively by observing both deep sleep and REM sleep duration, subjects sleep better without

the humidifier, with air conditioning turn on, light off and good air ventilation. Although, this is not conclusive enough to suggest the best ambient parameter condition for all cases since sleep preferences vary from one person to another and their preferences on the ambient setting night also are influenced by many reasons that are open for future investigation.

4.0 CONCLUSION

This study demonstrates the optimization version of a sleep monitoring system that relates in between surrounding ambient parameters and body vital condition for sleep quality study. Although the presented result is still premature and requires a deep investigation on four elements of ambient that can contribute to the sleep overall sleep quality, the presented result is decisive enough to conclude that the surrounding ambient is impacting the quality of sleep. From the sleep stage and the duration of time in each of the sleep stages, sleep quality and the better surrounding environment for sleeping can be determined. Based on the result of the four sets of experiments, the suitable room ambient to get a better night quality sleep with the temperature slightly lower than normal room temperature, minimalise the use of a humidifier, low intensity of light with all the lamp switch off and lastly with good airflow to the room indicating good air ventilation.

5.0 ACKNOWLEDGMENTS

Authors would like to thank the Machine Learning & Signal Processing (MLSP) research group under Fakulti Kejuruteraan Elektronik dan Kejuruteraan Komputer (FKEKK), of Universiti Teknikal Malaysia Melaka (UTeM) for sponsoring this work under project PJP/2020/FKEKK/PP/S01788 and providing the use of the existing facilities to complete this project.

6.0 REFERENCES

[1] V. V. Vyazovskiy, "Sleep, recovery, and metaregulation: explaining the benefits of sleep," *Nature and science of sleep*, vol. 7, p. 171, 2015.

[2] J. W. Kantelhardt, T. Penzel, S. Rostig, H. F. Becker, S. Havlin, and A. Bunde, "Breathing during REM and non-REM sleep: correlated versus uncorrelated behaviour," *Physica A: Statistical Mechanics and its Applications*, vol. 319, pp. 447–457, 2003.

[3] J. W. Burns, F. B. Consens, R. J. Little, K. J. Angell, S. Gilman, and

R. D. Chervin, "EMG variance during polysomnography as an assessment for REM sleep behavior disorder," *Sleep*, vol. 30, no. 12, pp. 1771–1778, 2007.

[4] R. Ferri *et al.*, "A quantitative statistical analysis of the submentalis muscle EMG amplitude during sleep in normal controls and patients with REM sleep behavior disorder," *Journal of sleep research*, vol. 17, no. 1, pp. 89–100, 2008.

[5] M. Baboli, A. Singh, B. Soll, O. Boric-Lubecke, and V. M. Lubecke, "Good night: Sleep monitoring using a physiological radar monitoring system integrated with a polysomnography system," *IEEE Microwave Magazine*, vol. 16, no. 6, pp. 34–41, 2015.

[6] A. Mamelak and J. A. Hobson, "Nightcap: a home-based sleep monitoring system," *Sleep*, vol. 12, no. 2, pp. 157–166, 1989.

[7] W. H. M. Saad, C. W. Khoo, S. I. A. Rahman, M. M. Ibrahim, and N. H. M. Saad, "Development of sleep monitoring system for observing the effect of the room ambient toward the quality of sleep," *IOP Conf. Ser.: Mater. Sci. Eng.*, vol. 210, p. 012050, Jun. 2017, doi: 10.1088/1757-899X/210/1/012050.

[8] F. Lin *et al.*, "SleepSense: A noncontact and cost-effective sleep monitoring system," *IEEE transactions on biomedical circuits and systems*, vol. 11, no. 1, pp. 189–202, 2016.

[9] W. H. bin Mohd Saad *et al.*, "Study on the Effect of the Ambient Temperature toward the Quality of Sleep," *IJECE*, vol. 7, no. 6, p. 2986, Dec. 2017, doi: 10.11591/ijece.v7i6.pp2986-2992.

[10] K. P. Wright Jr, C. Gronfier, J. F. Duffy, and C. A. Czeisler, "Intrinsic period and light intensity determine the phase relationship between melatonin and sleep in humans," *Journal of biological rhythms*, vol. 20, no. 2, pp. 168–177, 2005.

[11] P. Batog and M. Badura, "Dynamic of Changes in Carbon Dioxide Concentration in Bedrooms," *Procedia Engineering*, vol. 57, pp. 175–182, Jan. 2013, doi: 10.1016/j.proeng.2013.04.025.

[12] X. Xu *et al.*, "Experimental study on sleep quality affected by carbon dioxide concentration," *Indoor air*, vol. 31, no. 2, pp. 440–453, 2021.

[13] X. Zhang, G. Luo, J. Xie, and J. Liu, "Associations of bedroom air temperature and CO2 concentration with subjective perceptions and sleep quality during transition seasons," *Indoor air*, 2021.

[14] J. Xiong, L. Lan, Z. Lian, and R. De Dear, "Associations of bedroom temperature and ventilation with sleep quality," *Science and Technology for the Built Environment*, vol. 26, no. 9, pp. 1274–1284, 2020.

[15] S. I. Jang, J. Han, M. Lee, J. Seo, B. J. Kim, and E. Kim, "A study of skin characteristics according to humidity during sleep," *Skin Research and Technology*, vol. 25, no. 4, pp. 456–460, 2019.

[16] J. E. Lehto *et al.*, "Circadian preferences and sleep in 15-to 20-year old Finnish students," *Sleep Science*, vol. 9, no. 2, pp. 78–83, 2016.

[17] İ. Önder, Ş. Beşoluk, M. İskender, E. Masal, and E. Demirhan, "Circadian preferences, sleep quality and sleep patterns, personality, academic motivation and academic achievement of university students," *Learning and Individual Differences*, vol. 32, pp. 184–192, 2014.

Penumbra™

62

68

72

RED™

REPERFUSION CATHETERS

REDglide™ Technology
Designed to enhance delivery in tortuosity

62
.062" ID
1.93mm (0.76") OD
138cm Length

68
.068" ID
2.13mm (0.84") OD
132cm Length

72
.072" ID
2.16mm (0.85") OD
132cm Length